POLITECNICO
MILANO 1863

SCUOLA DI INGEGNERIA INDUSTRIALE
E DELL'INFORMAZIONE

Synthesis and characterization of thin film silicon oxycarbide for integrated optical thermal actuators

Tesi di Laurea Magistrale in
Materials Engineering and Nanotecnology -
Ingegneria dei Materiali e delle Nanotecnologie

Author: **Mattia Guastalla**

Student ID: 971082
Advisor: Prof. Andrea Ivano Melloni
Co-advisors: Oscar Adrian Jimenez Gordillo, Francesca Grossi
Academic Year: 2022-23

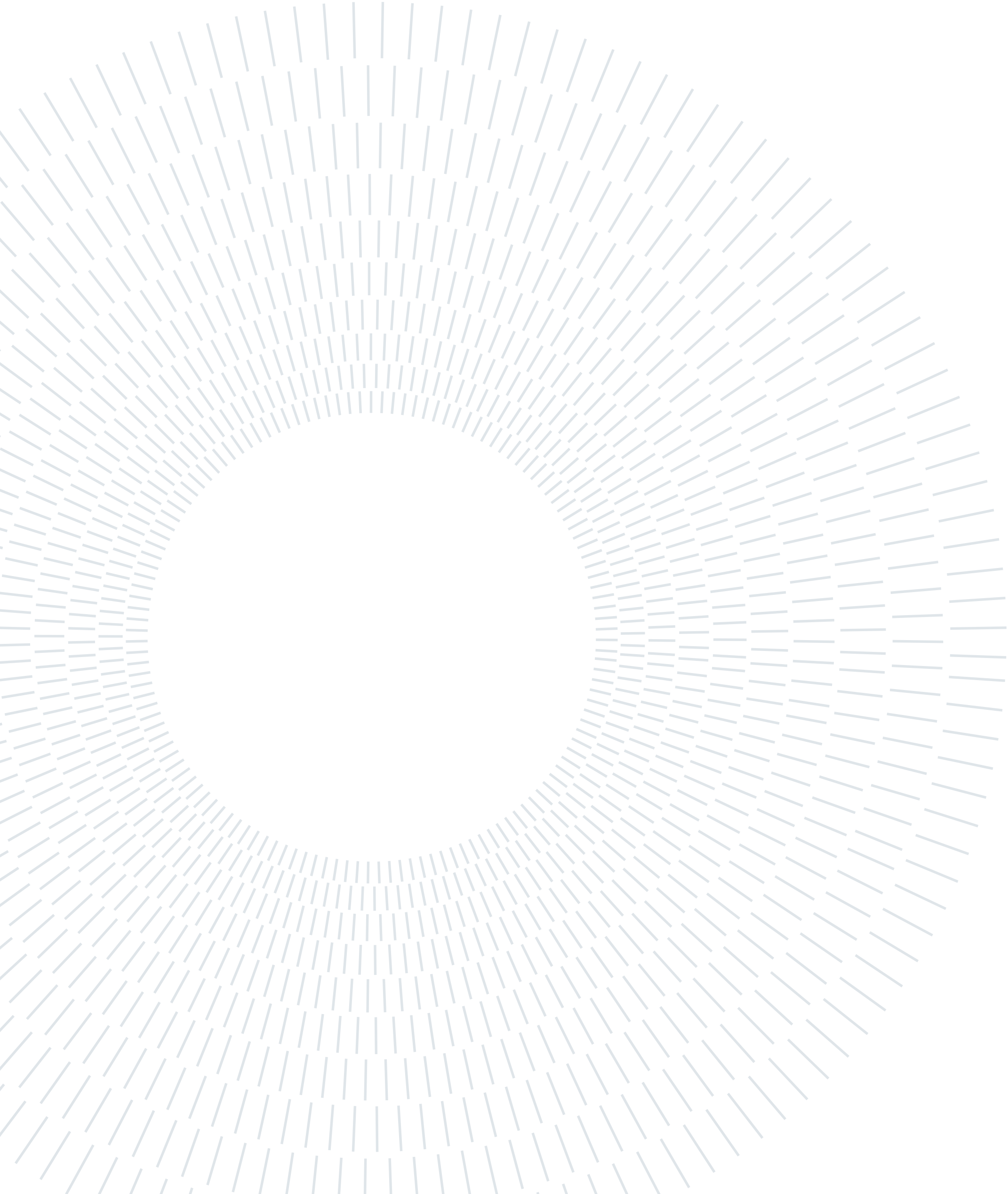

Abstract

This thesis work is focused on synthesizing, characterizing, and integrating sputtered thin films of silicon oxycarbide to realize efficient integrated optical thermal actuators. The SiOC composition should guarantee a very low absorption, a relatively high refractive index, the highest thermo-optic coefficient possible, and excellent adhesion to the typical materials used in integrated optical platforms. To this aim, the optical, morphological, and chemical properties change with the sputtering deposition have been analyzed. The integration of silicon oxycarbide on a silicon nitride waveguide with polymeric cladding has been investigated. Therefore a sputtering process has been developed to deposit sputtered thin films with a polymeric component integrated into the chip allowing the possibility to use of an enormous class of materials. The experimental evaluation of the thermo-optic coefficient through reflectometry of thin film silicon oxycarbide and directly on-waveguide shows a value as high as 2.6×10^{-4} °C^{-1}.
This work has been developed at Polifab clean room facilities, the micro and nanotechnology center of Politecnico di Milano, and at the Photonic Devices lab of Politecnico di Milano.

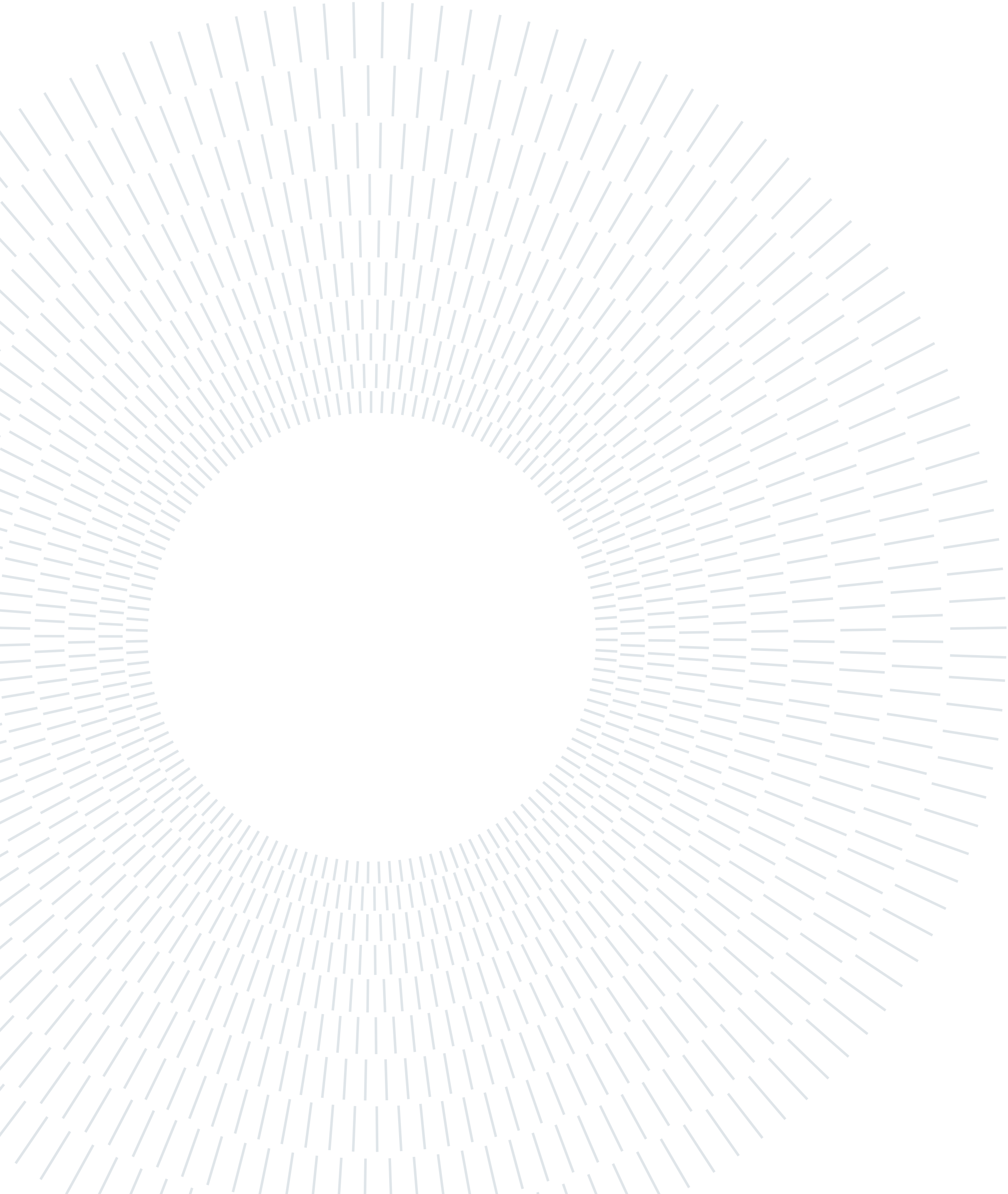

Sommario

Questo lavoro di tesi è incentrato sulla sintesi, caratterizzazione e integrazione di film sottili sputterati di ossicarburo di silicio per realizzare attuatori termici in ottica integrata efficienti. La composizione del SiOC dovrebbe garantire un assorbimento molto basso, un indice di rifrazione relativamente alto, il più alto coefficiente termo-ottico possibile e un'ottima adesione ai materiali tipici utilizzati nelle piattaforme di ottica integrata. A questo scopo sono state analizzate la variazione delle proprietà ottiche, morfologiche e chimiche con la deposizione per sputtering. È stata studiata l'integrazione di ossicarburo di silicio su una guida d'onda di nitruro di silicio con rivestimento polimerico. Perciò è stato sviluppato un processo di sputtering per depositare film sottili sputterati consentendo la possibilità di utilizzare un'enorme classe di materiali. La valutazione sperimentale del coefficiente termo-ottico tramite riflettometria di film sottili di ossicarburo di silicio e direttamente in guida d'onda mostra un valore fino a 2.6×10^{-4} $°\mathrm{C}^{-1}$.
Questo lavoro è stato sviluppato presso le camere bianche di Polifab, il centro di micro e nanotecnologie del Politecnico di Milano, e al Photonic Devices lab del Politecnico di Milano.

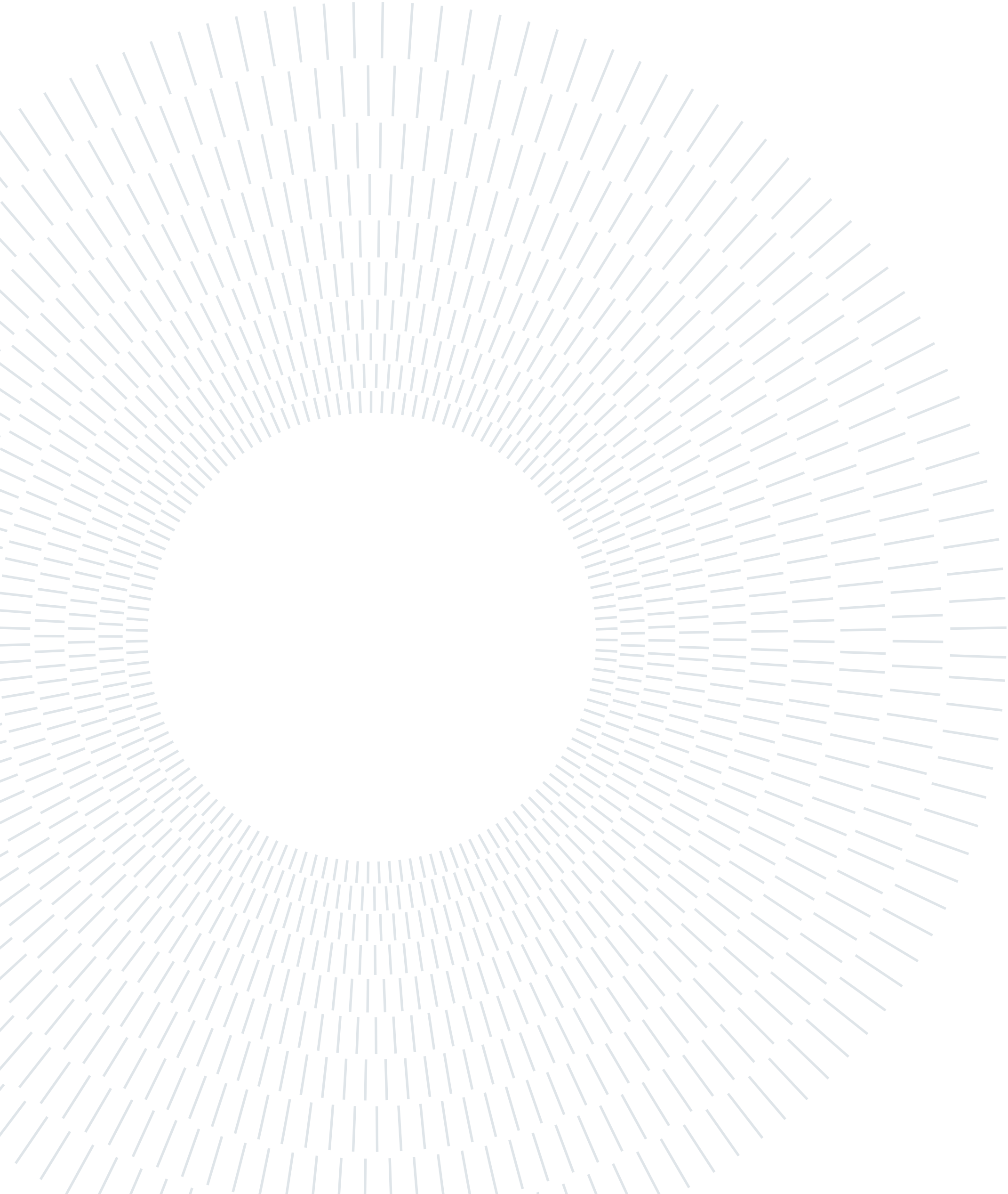

Contents

List of Figures

List of Tables

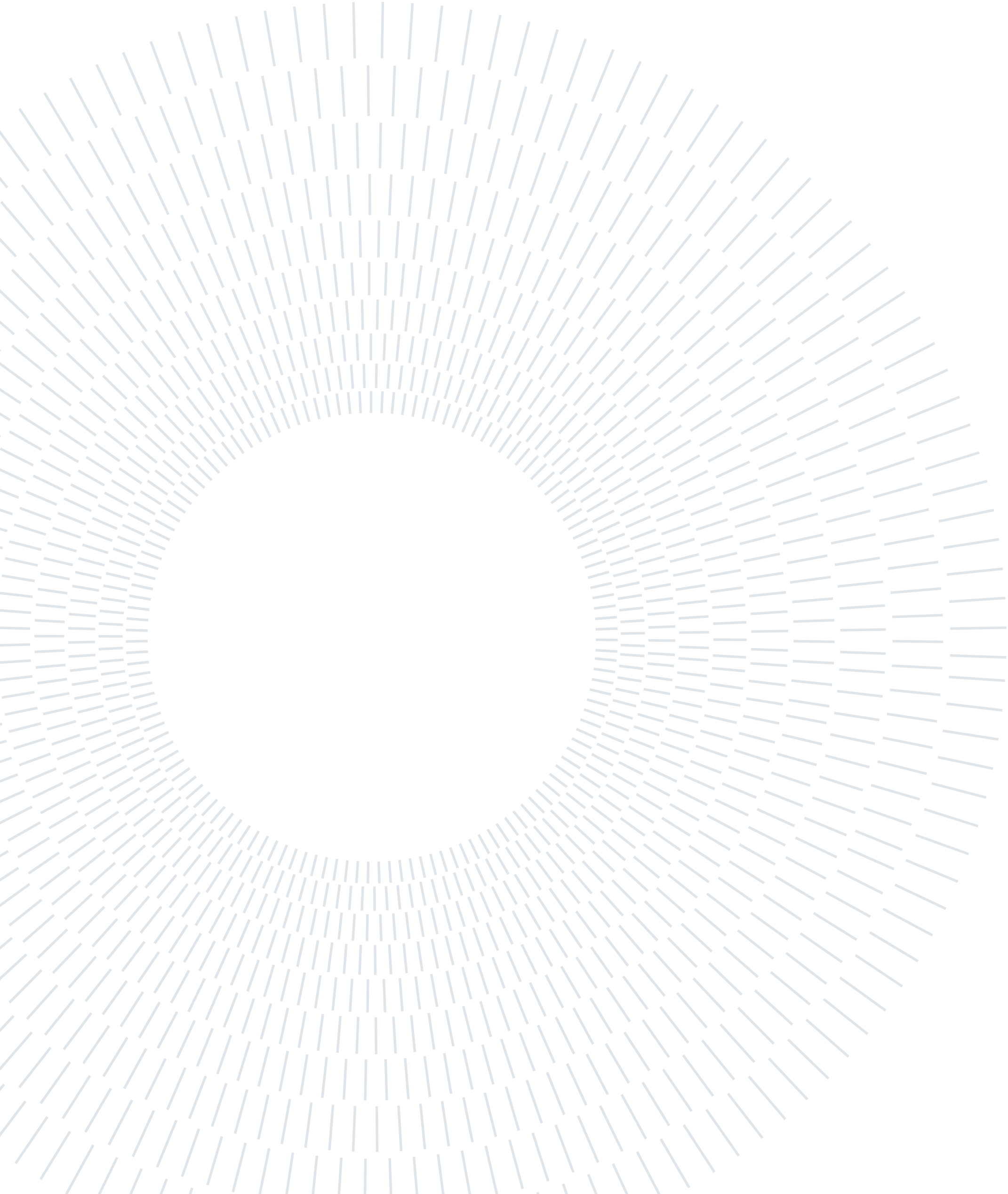

1 | Introduction

1.1. Integrated optics

Integrated optics is a technology that has emerged as a highly significant and increasingly important field, particularly in areas such as telecommunications [14], sensing [6], medicine [7], and more. The focus of integrated optics is the study of light-matter interaction and aims to incorporate optical devices onto a chip. This integration of optical components onto a chip is fundamental for achieving miniaturization, scalability, and low costs [2] of production within a compact space. Moreover, integration has great advantages regarding CMOS compatibility with microelectronic devices. In general, the progression of integrated optics has changed the field of photonics, enabling the integration of optical components and functionalities onto a chip, such as lasers, semiconductor detectors, and modulators which are very important as active components.

The building block of the integrated photonic chip is the waveguide, a dielectric passive component responsible for guiding the electromagnetic wave using the total internal reflection conditions. Depending on the application, the waveguide is some millimeter longer and thickness between the hundreds of nanometers to some μm. Based on the wavelength used, the waveguide must be made with a lossless material with a high refractive index contrast to confine the wave. With the waveguide, it is possible to build some crucial devices like filters, grating, interferometers, couplers, polarizers, etc.

The material selection for the integrated optics is really important. For active components, the most popular are semiconductors of the III-IV groups like indium phosphide (InP) to make lasers or gallium arsenide (GaAs) to make detectors or lithium niobate ($LiNbO_3$) to exploit the electro-optic effect for modulators. For the cladding silicon oxide is used because of its chemical and thermal stability. Also, polymers are used as cladding materials because they are easy to process thanks to the lithography process. A lossless material at those wavelengths and with a high refractive index contrast is needed to guide the light in a waveguide. One of the most popular materials is silicon because of its transparency in the telecommunication range, high refractive index, low cost, and CMOS compatibility. Another popular material to make a waveguide is silicon nitride which is used to exploit a different wavelength range such as the visible or exploit non-linear optic effects, such as thermal and Kerr properties [15]. Silicon nitride is an excellent alternative to silicon because it is CMOS-compatible, has low propagation losses, and has good thermal stability.

1.2. Thermal actuators

To obtain optical modulation in integrated optics technology a change of the optical field is needed. To obtain the optical modulation, we have to shift the phase of the wave in the integrated optical device. The phase shift is related to the following formula:

$$\Delta\phi = \frac{2\pi}{\lambda}\Delta n_{eff}\Delta L \tag{1.1}$$

Thus, to change the phase of a wave in the device we can induce a change in the refractive index or in the device length. The actuators are devices that allow tuning, dynamic control, and reconfigurability of the properties of the optical system, like the refractive index, to provide phase shift. There are several types of actuators based on the effect we want to exploit. For example, the p-n junction exploits the carrier injection or depletion of a silicon waveguide to change the refractive index [29], or a MEMS-based actuator that enables functionalities such as wavelength tuning, optical switching, or optical scanning [12]. But one of the most popular is the thermal actuator which provides phase shifting of a wave changing the refractive index of the waveguide through temperature with the following formula:

$$\Delta n_{eff} = K_T\Delta T \tag{1.2}$$

where the K_T is the thermo-optic coefficient and it is the material property exploited for the development of the thermal actuator device. To heat the thermal actuator, an electrical metal resistor typically heats up the thermo-optic material to a desired temperature. Thermal actuators are really popular in integrated optics because they are easy to fabricate with respect to the carrier injection method as it is required only an increase of temperature through metallic pads, are reliable, are compact, CMOS-compatible, and have low power consumption [13]. The thermal actuator comprises metallic pads, which will cede heat through Joule's effect, and the high thermo-optic material structure responsible for the phase shift. The thermo-optic material structures can be waveguides in the case of silicon (thermo-optic coefficient 1.86×10^{-4} °C^{-1}) as shown in Figure 1.1 or a strip of some hundred nm where and with a length chosen to phase shift a wave of π radiants with a determined ΔT (typically some μm), put upon the waveguide to cover and maximize the interaction of the modes. In Table 1.1 are listed some of the most popular materials used in photonics. In the case of the silicon nitride platform, the thermo-optic is really low (2.51×10^{-5} $^\circ C^{-1}$), so a strip of high thermo optic material, CMOS-compatible and with higher refractive index is needed. To have an efficient thermal actuator device the high thermo-optic material selection is needed to provide phase shift with the lower power consumption possible.

Material	**Thermo-optic coefficient $^\circ \mathbf{C}^{-1}$**
Crystalline silicon	1.86×10^{-4}
Amorphous silicon	2.4×10^{-4}
Silicon nitride	2.51×10^{-5}
Silicon oxynitride	1.1×10^{-5}
Silicon oxide	1×10^{-5}
SU8 photoresist	-1.1×10^{-4}

Table 1.1: Some thermo-optic coefficients of popular photonic materials [19]

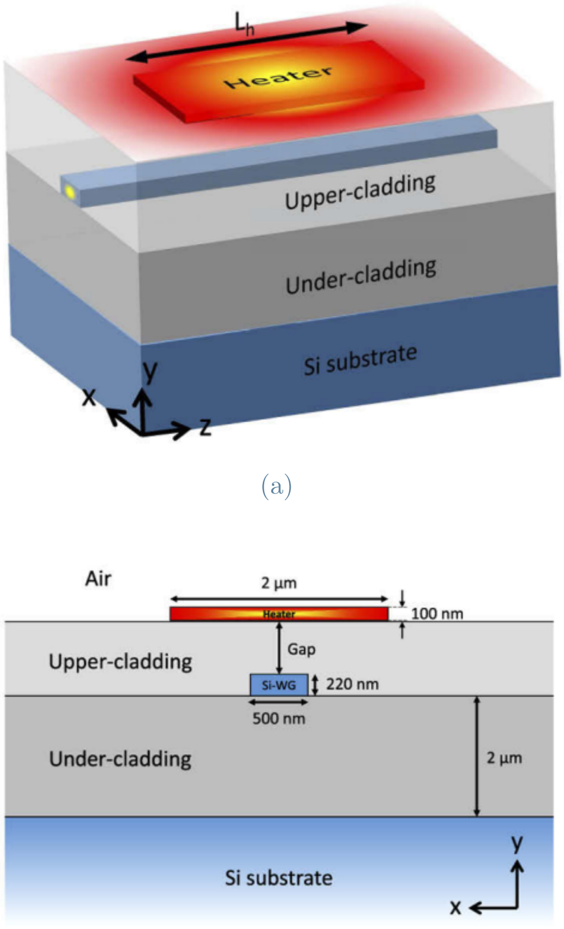

(a)

(b)

Figure 1.1: In (a) 3D view schematic and (b) cross-section of the analyzed heater/Si waveguide configuration [26].

1.2.1. Silicon oxycarbide

The silicon oxycarbide is a promising candidate material for thermal actuator devices in IR window wavelengths, because of its transparency over the IR wavelength range, high thermo-optic coefficient (2.5×10^{-4} °C^{-1}, $\approx 30\%$ more with respect silicon), it is possible to tune the refractive index and it is CMOS-compatible [18]. SiOC is a glassy material wherein oxygen and carbon atoms share bonds with silicon in the amorphous, network structure. There are several ways to obtain this material, among which are the sol-gel solution [25], PECVD [35], PVD-Sputtering [18], and poly-siloxane pyrolysis [5].

1.3. Thesis objectives and contribution

The main objective of the thesis is to develop a reproducible high-quality thin film silicon oxycarbide with a high thermo-optic coefficient, and a refractive index of ≈ 2.2 and integrate it into an integrated photonic platform. As we said before the silicon nitride platform has low thermo-optic coefficient, so the silicon oxycarbide is needed to provide the thermal actuation of the signal in the waveguide. To have the interaction with the light in the silicon oxycarbide we deposit on top a thin layer with a refractive index with respect to the silicon nitride waveguide ($n \approx 2$).

This work contains some original contributions that are listed below:

- Integration of silicon oxycarbide on-chip with a polymeric cladding
- Experimental and characterization of the thermo-optic coefficient through reflectometry experiment on thin film

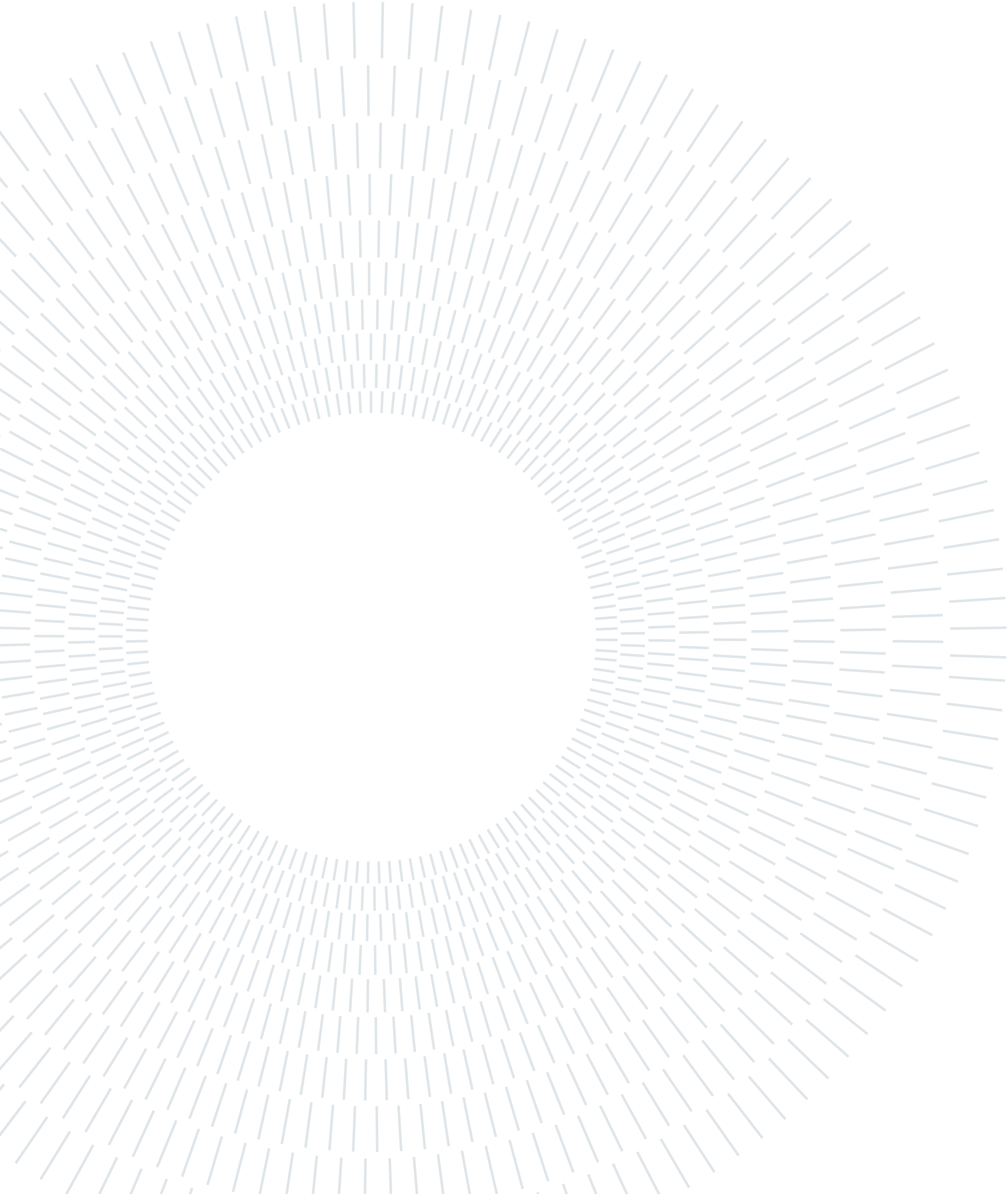

2 | SiOC deposition

2.1. Physical Vapor Deposition: Sputtering

This work will synthesize the silicon oxycarbide with PVD: Sputtering method through silicon carbide basis and exploiting the reaction with oxygen-reactive gas. The sputtering process is ideal to make pure thin films, controlling the optical properties efficiently by adjusting only a few parameters. Physical vapor deposition (PVD) is a set of atomistic deposition techniques in which material is vaporized from a solid or liquid source in the form of atoms or molecules and transported through a vacuum or low-pressure gaseous (or plasma) environment to the substrate, where it condenses [17]. Typically, PVD processes are used to deposit films with thicknesses ranging from a few nanometers to thousands of nanometers. Among these technologies, the sputtering process is one of the most widely used thin-film fabrication techniques in diverse industries such as semiconductor processing, surface finishing, and jewelry making [16]. This technique is based on the physical vaporization of atoms from a surface through momentum transfer from energetic positive ions generated by a plasma. The sputtering system utilized in this process includes a vacuum chamber, a target plate made of the desired deposition material, a substrate plate where the material is deposited, a power supply, and gas valves. These components work together to generate a plasma discharge and enable the option for reactive deposition. Typically, the sputtering gas used for plasma generation is Ar at a pressure less than 10^{-6} mbar [17]. Following the application of a voltage between the two plates, electrons are dissociated from the gas molecules, generating positively charged ions. Once this voltage surpasses a specific threshold, these ions are accelerated through the potential drop towards one of the two plates (which will behave as a cathode), leading to the physical evaporation of particles from the target material. Subsequently, these particles are deposited onto the substrate plate (which will behave as an anode). The characteristics of the glow discharge play a significant role in this deposition method and are primarily influenced by the target's geometry, the target material, and the gases employed. The entire process is illustrated in Figure 2.1

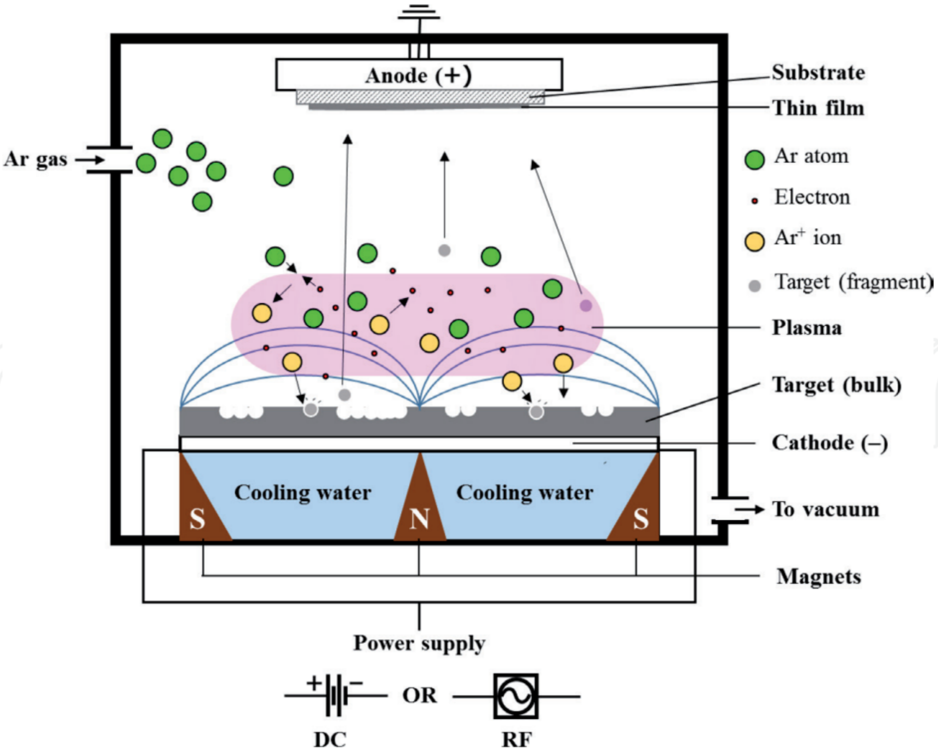

Figure 2.1: Simple image of how the sputtering works

2.1.1. RF Sputtering

As the silicon oxycarbide is an insulator, applying a direct current on a silicon carbide target is not ideal: the negative voltage needed to generate a glow discharge would be too high because of the high resistivity of the target. The solution to this problem is to apply a high-frequency alternate voltage instead of a DC. If the frequency is ≈ 1 MHz, the electrons will move back and forth between the target and the substrate causing ionizing collision and, therefore, the expansion of the plasma and sheath regions [24]. But the AC voltage could induce the sputtering of both the cathode. To avoid this possibility, it is convenient to design properly the dimensions of the cathodes [24].

2.1.2. Reactive Sputtering

Silicon oxycarbide is a compound material of silicon carbide when chemical reactions with O_2 occur. Thus, among the sputtering technologies, the reactive one is the desired one. The reactive sputtering works when a compound thin film is wanted, so it is possible to use reactive gasses (in this case only O_2) mixed with the inert one to induce a chemical reaction near the target material. If the reactive gas flux is too high the target will be poisoned because the compound layer will cover the surface. It causes a decrease in the cathode voltage and the deposition rate leading to a hysteresis effect [24]. It is imperative to avoid this effect on our deposition process; otherwise, it will form a layer of silicon oxide on the silicon carbide target surface, making the deposition of silicon oxycarbide impossible.

2.2. Machine and process overview

2.2.1. Sputtering system

The RF magnetron sputtering system employed to deposit silicon oxycarbide films (SiOC) was the LH Z400 MS system, developed by Leybold-Heraeus (Figure 2.2). The system includes a vacuum chamber with three cathode target sites (Figure 2.3), each of them has a different sputtering configuration, namely DC, RF, and magnetron. Only the RF configuration is used for this experiment, which corresponds to the second cathode site. As a target, we used a silicon carbide (SiC) with a diameter of 4 inches, supplied by Ajaint Inc. To protect the targets, each target is enclosed within a cylindrical container. This container allows for the capability to seal and close it when a target is not in use. To avoid contamination, the container must be kept closed during deposition runs. Rotary and turbo-molecular pumps were employed in parallel to achieve the desired vacuum. To reach vacuum condition, the rotary pump reaches a vacuum of 5×10^{-2} mbar which is needed to use the turbo-molecular to reach a vacuum pressure of 10^{-6} and below. A gate valve is employed to regulate the aperture of the turbo-molecular pump. We utilize two types of vacuum gauges to monitor and control the pressure within the system. The first is a capacitance vacuum gauge, which allows us to measure pressure values up 10^{-4} mbar. While for values even lower, an ionization vacuum gauge is used. The flow of oxygen and argon gases during the deposition process was controlled by an (MKS 147B four-channel controller running two 1159B) mass-flow controllers.

Figure 2.2: Sputtering system - Leybold LH Z400 MS

The substrate holder is mounted upside down on a stage to avoid any contaminants which can detach from the walls of the containers. We can rotate the stage manually through a control crank to move the sample to the desired cathode. The distance between the target and the substrate was kept constant at 60 mm for all deposition runs. The process parameters are set through a control panel and include:

- RF power which points out the intensity of the plasma in the chamber
- Flow rate of the Ar to generate the plasma
- Flow rate of O_2 for a reactive option
- DC Bias voltage to avoid the ion bombardment of the substrate
- Capacities CT and CL to minimize the reflected power of the process

In this study, silicon oxycarbide films were deposited by introducing argon (Ar) and oxygen (O_2) gases into the system and applying RF power. The values of these parameters were systematically changed across a wide range to investigate their impacts on the deposited films' morphology, topography, and optical properties.

(a) (b)

Figure 2.3: In 2.3a the vacuum chamber of the sputtering system with all of the three cathode sites. In 2.3b the silicon carbide target

2.2.2. Process

The deposition process of silicon oxycarbide thin films was carried out on square pieces of 2X2 cm, used as substrates, obtained from a 6-inch monocrystalline silicon wafer Si <100> (Figure 2.6). These square pieces were cut using a diamond point engraver to achieve the desired geometry. Before the deposition process, it is necessary to perform a cleaning step on the samples to eliminate any organic contaminants that could negatively impact the quality of the thin films. The cleaning procedure involves immersing the samples in acetone followed by isopropyl alcohol (IPA). Subsequently, the samples were dried with a nitrogen gas gun to remove any remaining residues. Finally, all chemicals are removed using oxygen (O_2) plasma generated by a Plasma Asher (Figure 2.4).

Figure 2.4: Plasma asher machine as last cleaning step of the samples substrates (PVA TEPLA 300 AL)

To introduce the samples in the sputtering system the substrates were attached to a 6-inches metallic circular sample holder with metallic clamps at the edges (Figure 2.6) After mounting the holder in the chamber, we have to pump down the system to a vacuum pressure of 10^{-6} and lower. To turn on the plasma we have to put the Ar gasses in the chamber through the control panel while lowering the aperture of the turbo-molecular pump through the gate valve until the value of pressure is at 1.1×10^{-2} mbar. Due to the susceptibility of the SiC target to atmospheric exposure, a process to maintain its purity before each deposition is needed. This process, called pre-sputtering, consists of turning on the plasma at the typical power of the deposition (280 W) for 10 minutes to clean the SiC target surface, removing any contaminants or oxide layers that may have formed during exposure to the atmosphere. During the pre-sputtering, the sample holder is not in front of the target to avoid the deposition of SiC onto the silicon substrates.

The target used is made of SiC and to obtain SiOC a reaction with oxygen is needed. During the deposition, part of the SiC target surface reacts with the oxygen, and if the last is present with a partial pressure of less than 1 bar the following chemical formula occurs [30]:

$$\mathrm{SiC} + \mathrm{O_2} \rightarrow \mathrm{SiO_2} + \mathrm{CO}$$

The reaction is strongly exothermal and favorable (reaction enthalpy $\Delta\mathrm{H} = -958.4$ kJ/mol at standard state [3]), so to decrease the kinetics a little quantity of oxygen is needed to not oxidize completely the target surface, therefore it's necessary to carefully control oxygen flow and concentration. The stoichiometric formula of the silicon oxycarbide is $SiO_{2(1-x)}C_x$, x is the carbon concentration and has to be included between 0<x<1 [5][23], so there are different possible compositions (Figure 2.5). To each different composition correspond different optical properties, so carbon concentration is the key parameter to obtain the thin film with the desired properties.

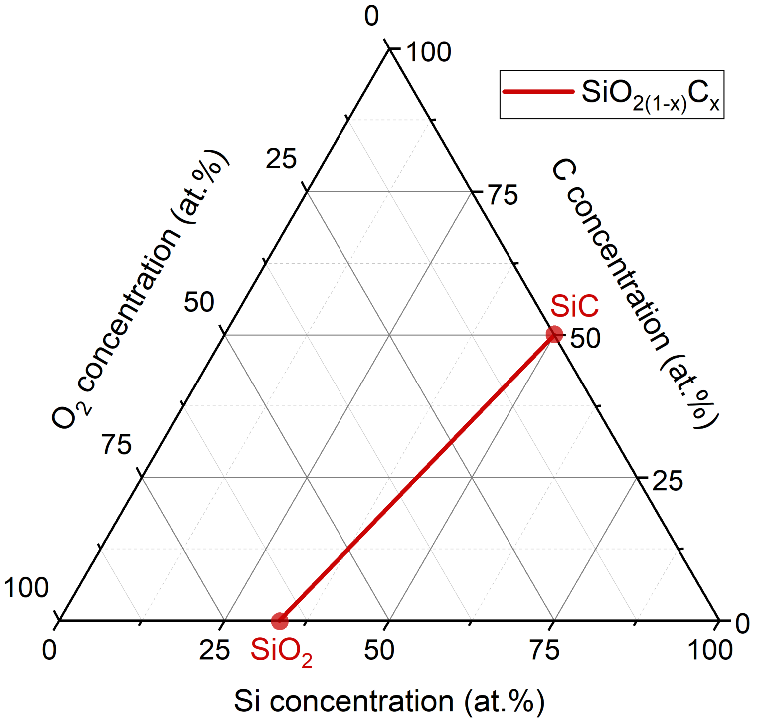

Figure 2.5: Ternary phase diagram for silicon oxycarbide, the solid line shows the possible composition of the stoichiometry $SiO_{2(1-x)}C_x$ thin film.

To obtain the SiOC films with the expected properties the impact of process parameters, such as O_2 and Ar gas flux, the vacuum pressure of the chamber, and RF power has been evaluated. Moreover, an analysis of the deposition rate has been made. The thickness of the thin films can vary depending on the specific deposition process employed.

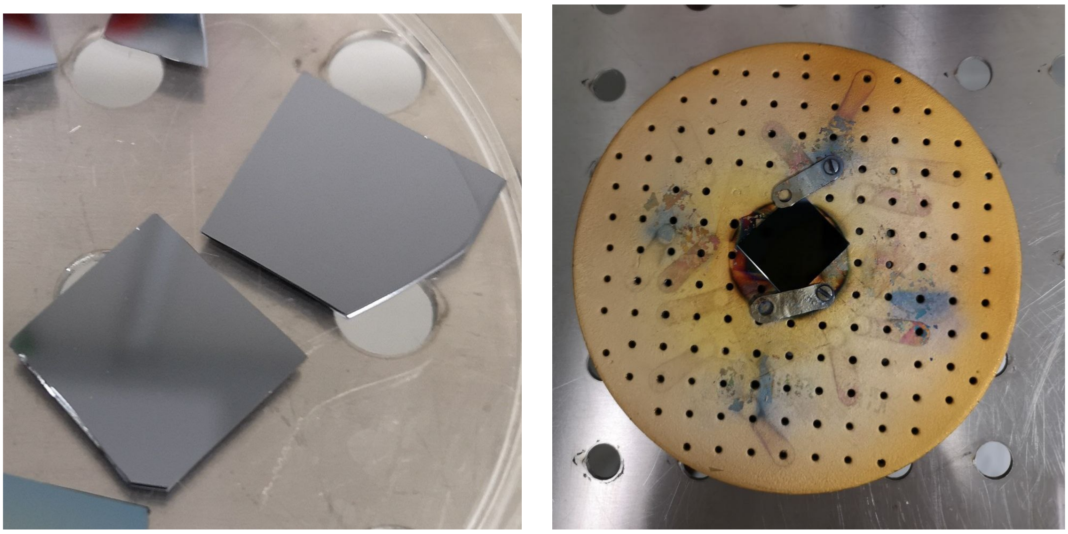

(a) (b)

Figure 2.6: In (a) Si <100> squares 2x2 cm before the deposition process, while in (b) Metallic circular sample holder with Si sample attached before the sputtering deposition

2.3. Film Characterization

2.3.1. Ellipsometry

The optical properties of the SiOC films, specifically the spectra of refractive index (n) and extinction coefficient (k), were determined using a variable angle spectroscopic ellipsometer (VASE J.A. Woollam Inc. USA). Ellipsometry is a technique employed to measure thin films' thickness and optical constants. It operates by examining the polarization state change of light reflected from the surface of the stack, film plus substrate, under investigation. The ellipsometer provides two measured quantities, namely Psi (Ψ) and Delta (Δ), which are defined as the parameters obtained from the ratio of the parallel polarized reflection coefficient r_p and normal polarized reflection coefficient r_s [10]. To characterize the SiOC films accurately, two angles of incidence were selected for the ellipsometry measurements: 70° and 75°. These angles were chosen to align with the Brewster angle of the silicon substrate (whose values span to 75.5° at 600 nm and 74° at 1550 nm)) to maximize the difference between the light polarized in p and in s, thus maximizing the signal received. The measurements were carried out over a spectral range from 600 nm to 1600 nm.

Fitting models were utilized to determine the thin film's optical properties. We referred to previous studies and employed pre-made models in the ellipsometer database. For SiOC film analysis, a pre-existing file based upon the Cody-Lorentz model. It was necessary to configure various parameters in the fitting mode to extract the optical properties from the optical response. This allowed the WVASE software to adjust the model curve to closely match the real response, as illustrated in Figure 2.7b.

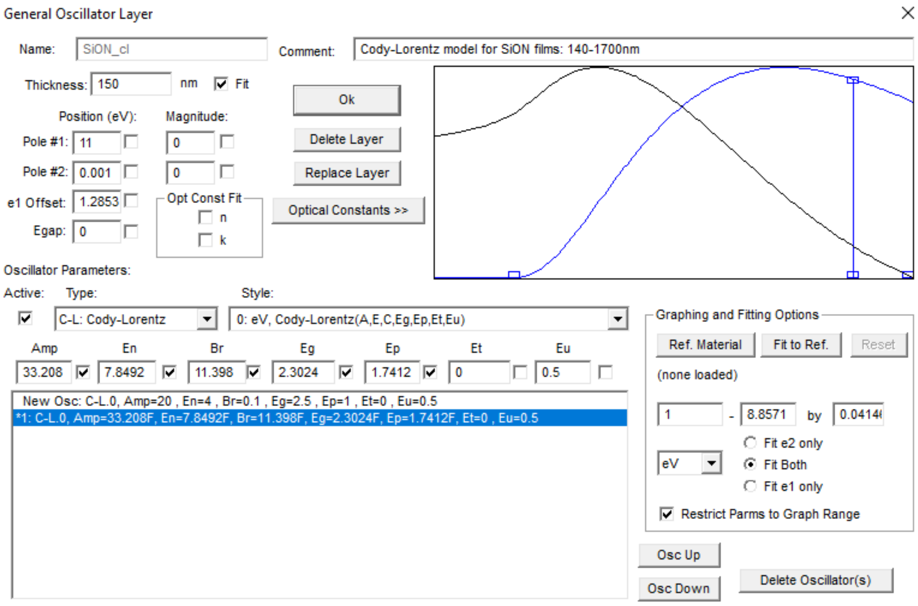

General Oscillator Layer

Name: SiON_cl

Comment: Cody-Lorentz model for SiON films: 140-1700nm

Thickness: 150 nm ☑ Fit

	Position (eV):		Magnitude:	
Pole #1:	11	☐	0	☐
Pole #2:	0.001	☐	0	☐
e1 Offset:	1.2853	☐		
Egap:	0	☐		

Opt Const Fit: ☐ n ☐ k

Oscillator Parameters:

Active: ☑ Type: C-L: Cody-Lorentz Style: 0: eV, Cody-Lorentz(A,E,C,Eg,Ep,Et,Eu)

Amp		En		Br		Eg		Ep		Et		Eu	
33.208	☑	7.8492	☑	11.398	☑	2.3024	☑	1.7412	☑	0	☐	0.5	☐

New Osc: C-L.0, Amp=20 , En=4 , Br=0.1 , Eg=2.5 , Ep=1 , Et=0 , Eu=0.5

*1: C-L.0, Amp=33.208F, En=7.8492F, Br=11.398F, Eg=2.3024F, Ep=1.7412F, Et=0 , Eu=0.5

Graphing and Fitting Options

(none loaded)

1 - 8.8571 by 0.0414

eV

○ Fit e2 only

● Fit Both

○ Fit e1 only

☑ Restrict Parms to Graph Range

(a)

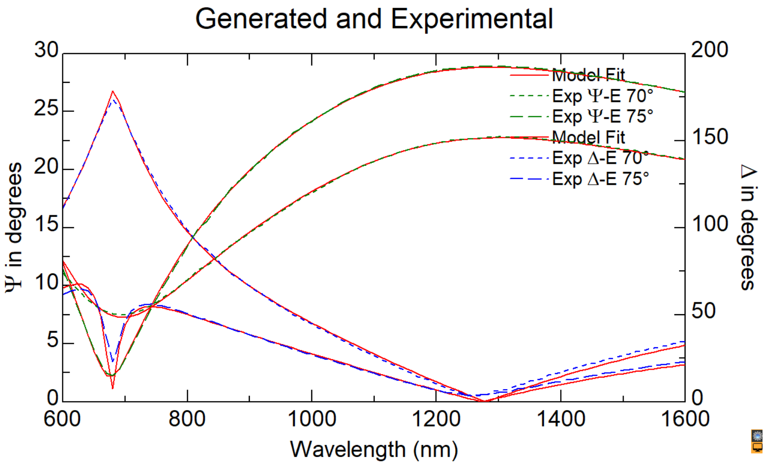

(b)

Figure 2.7: In (a) the software control panel of the fit, the v marks in the boxes are the fitting parameter. In (b) the spectra of the SiOC thin film, the dashed line is the real response of the material, while the solid line is the fitting model

In general, the SiOC-analyzed films have a percentage of refractive index gradient along the thickness. The values span from 3% to 20% with respect to the thickness (as shown in Figure 2.8). The refractive index decreases from top to bottom so we have to choose the optimal values of the process parameters to obtain a thin film with the lower value of the refractive index always higher than 2.0.

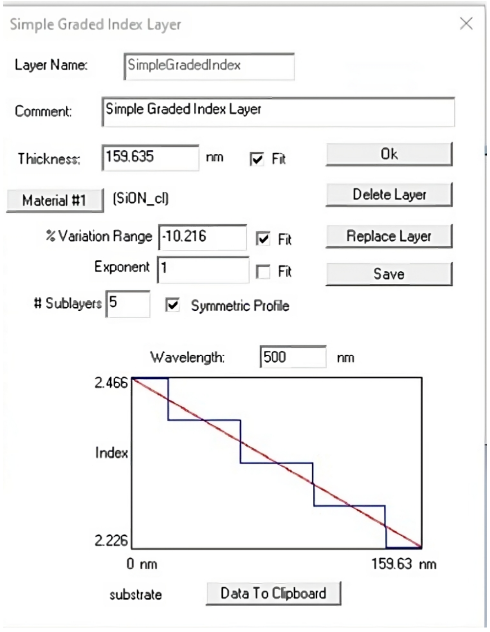

Layer Name: SimpleGradedIndex

Comment: Simple Graded Index Layer

Thickness: 159.635 nm ☑ Fit

Material #1 (SiON_cl)

% Variation Range -10.216 ☑ Fit

Exponent 1 ☐ Fit

Sublayers 5 ☑ Symmetric Profile

Wavelength: 500 nm

Figure 2.8: A panel of the WVASE software to see any refractive index gradient with respect to the thickness. The trend below represents how the refractive index change with the thickness

2.3.2. Profilometry and SEM analysis

To accurately determine the actual thickness of the deposited films, a profilometry analysis was performed using the KLA Tencor P-17 mechanical profilometer. In Figure 2.9 is shown the specific region selected to measure the thickness profile of the film. The measured thickness data of the sample from the ellipsometer is 558 nm. However, the scanned region was one of the edges of the sample and not the center. The thickness measured on the edges is 330 nm suggesting an increase of thickness up to the center. To obtain an accurate assessment of the center height of the film, a scanning electron microscopy (SEM) measurement was performed on the sample, as shown in Figure 2.17b. In order to obtain the thickness of the sample center, the sample was cleaved into two halves using a diamond engraver. As expected, the thickness measurements obtained from the SEM scan align with the results obtained from the ellipsometer.

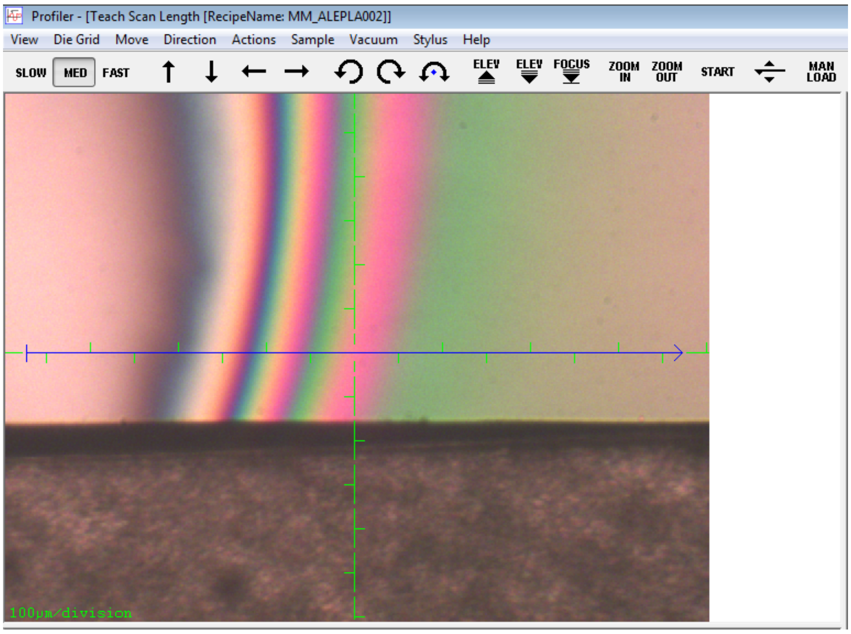

(a)

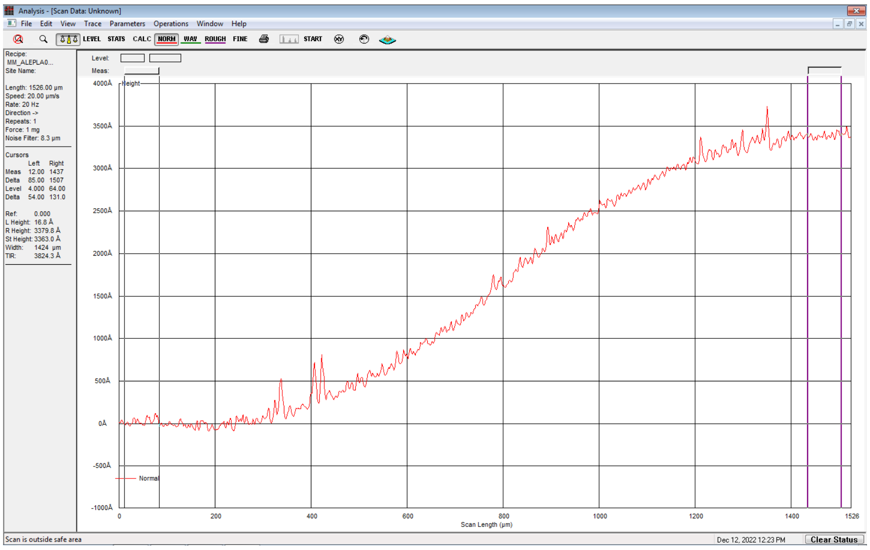

Recipe:
MM_ALEPLA0...
Site Name:

Length: 1526.00 µm
Speed: 20.00 µm/s
Rate: 20 Hz
Direction ->
Repeats: 1
Force: 1 mg
Noise Filter: 8.3 µm

Cursors

	Left	Right
Meas	12.00	1437
Delta	85.00	1507
Level	4.000	64.00
Delta	54.00	131.0

Ref: 0.000
L Height: 16.8 Å
R Height: 3379.8 Å
St Height: 3363.0 Å
Width: 1424 µm
TIR: 3824.3 Å

Scan is outside safe area

Dec 12, 2022 12:23 PM

(b)

Figure 2.9: In (a) the magnification of the zone used to measure the profile of the thin film. The pink zone is bare silicon and the green is the SiOC. While in (b) the profile of the thin film. The thickness measured is in the left side of the image and it is 337 nm.

A further SEM analysis was made to assess the compactness of the thin film. Upon examination, as shown in Figure 2.10b, it is evident that the thin film exhibits a compact structure without visible signs of porosity or defects that could potentially alter its properties. This observation suggests that the film possesses a uniform and dense structure, which is advantageous for maintaining the desired characteristics and performance.

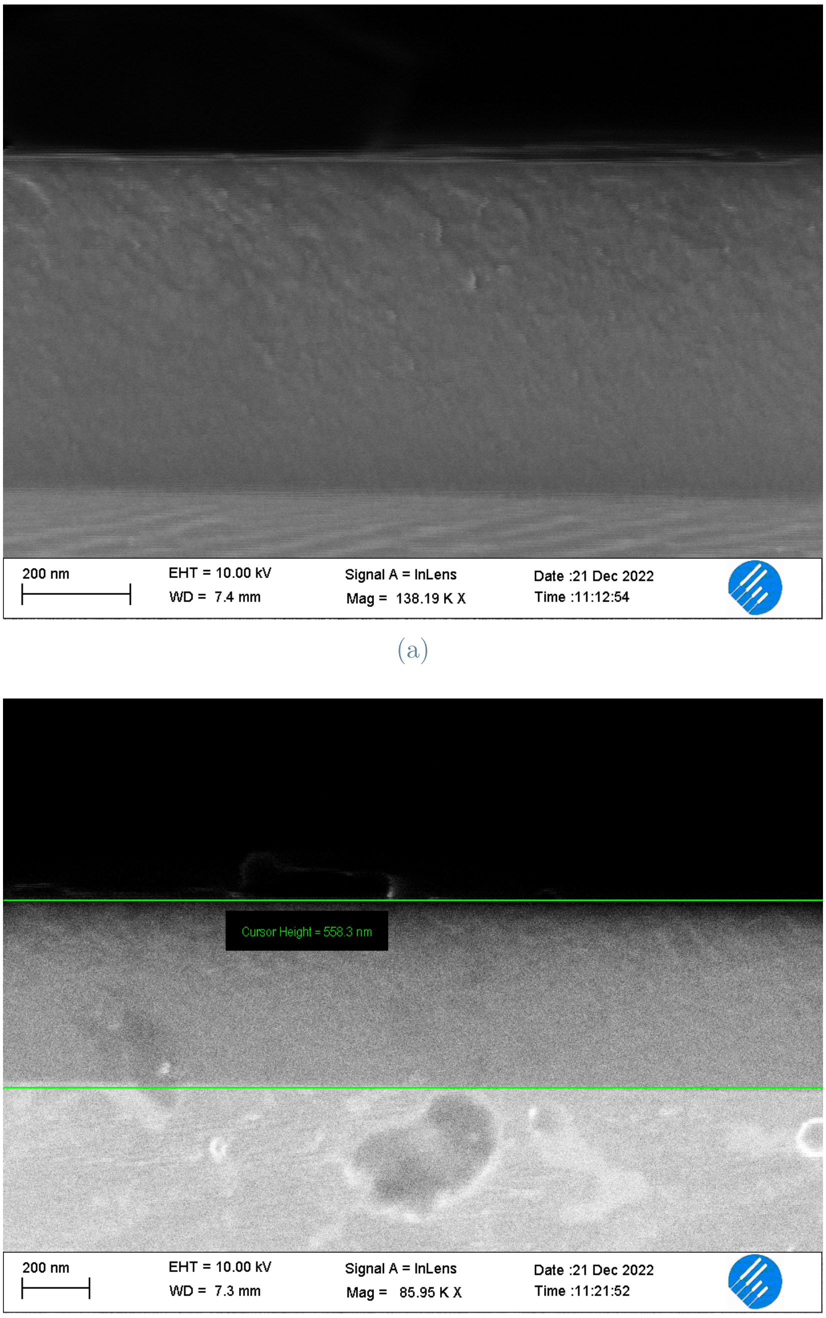

(a)

(b)

Figure 2.10: In (a) SEM scan of SiOC thin film 500 μm, the structure doesn't show any porosities or defects, while in (b) the thickness measurement of the thin film

2.3.3. EDX analysis

To assess the chemical composition of the film deposited with the developed process recipe an EDX analysis was performed. Energy Dispersive X-ray (EDX) microanalysis is a technique of elemental analysis associated with electron microscopy. It's based on the generation of characteristic X-rays that reveals the presence of elements present in the specimens. For this analysis, a film with a maximum thickness of 1.5 with a refractive index of 2.25 has been used. With this thickness, the images taken from SEM are not well defined, probably because silicon oxycarbide is considered an insulator it can accumulate charges. If instead, we deposit a gold layer of some nanometers through sputtering deposition (as shown in Figure 2.11) the silicon oxycarbide film is well visualized. The SEM scans of the thin film with gold and without gold are shown in Figure 2.12

Figure 2.11: The sputtering system to deposit gold on the sample, the violet shroud is the plasma for the deposition

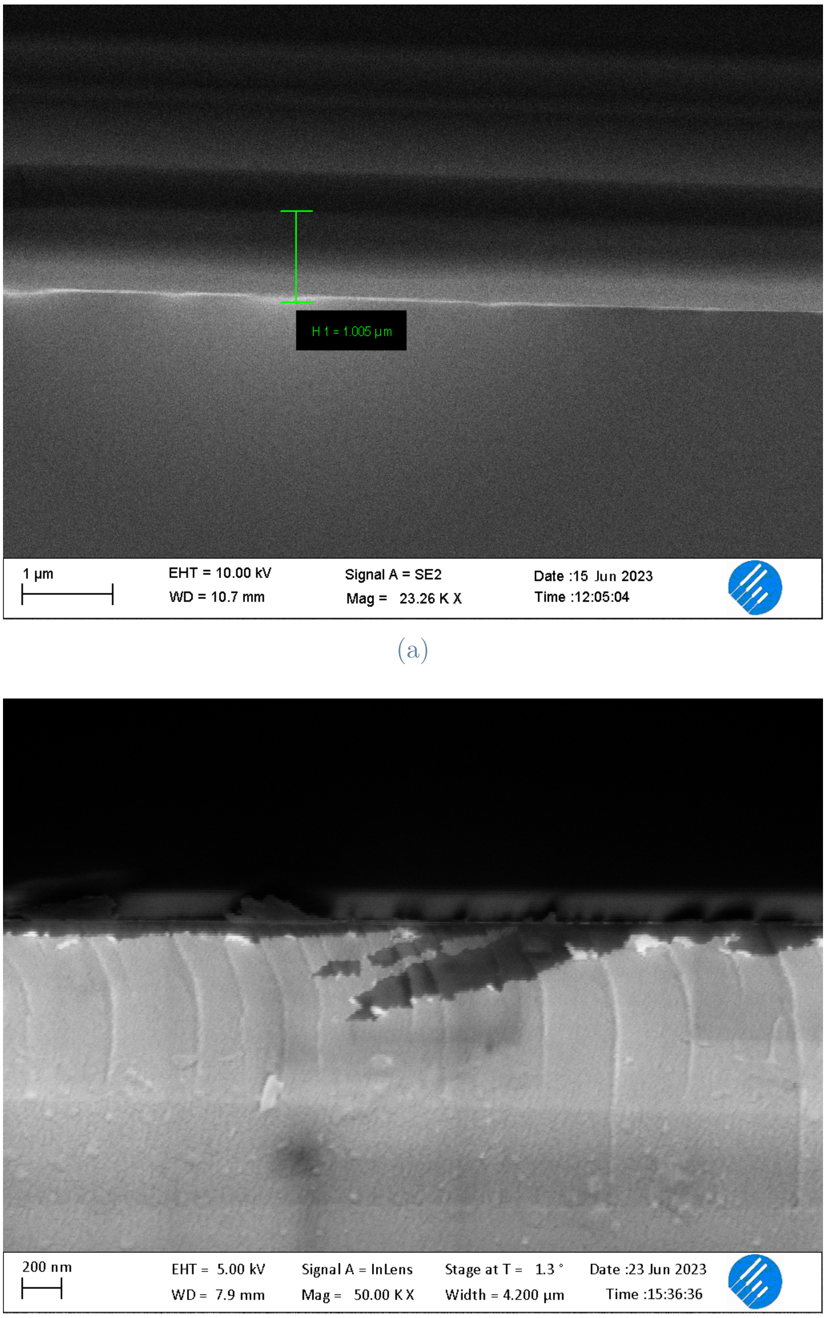

(a)

(b)

Figure 2.12: In (a) SEM scan of SiOC thin film of 1 μm, the image is so blurred because the thin film accumulates charges, while in (b) the same film with a gold layer 5 nm thick

For the EDX analysis, we select a scan area in which no gold is present, and the results of the chemical composition (in Table 2.1) of the thin film are visualized in Figure 2.13. The composition found doesn't follow perfectly the ternary state diagram (Figure 2.14), but the error is quite large, for this reason, a more precise analysis such as the XPS and SIMS it's required to confirm and assess the chemical composition.

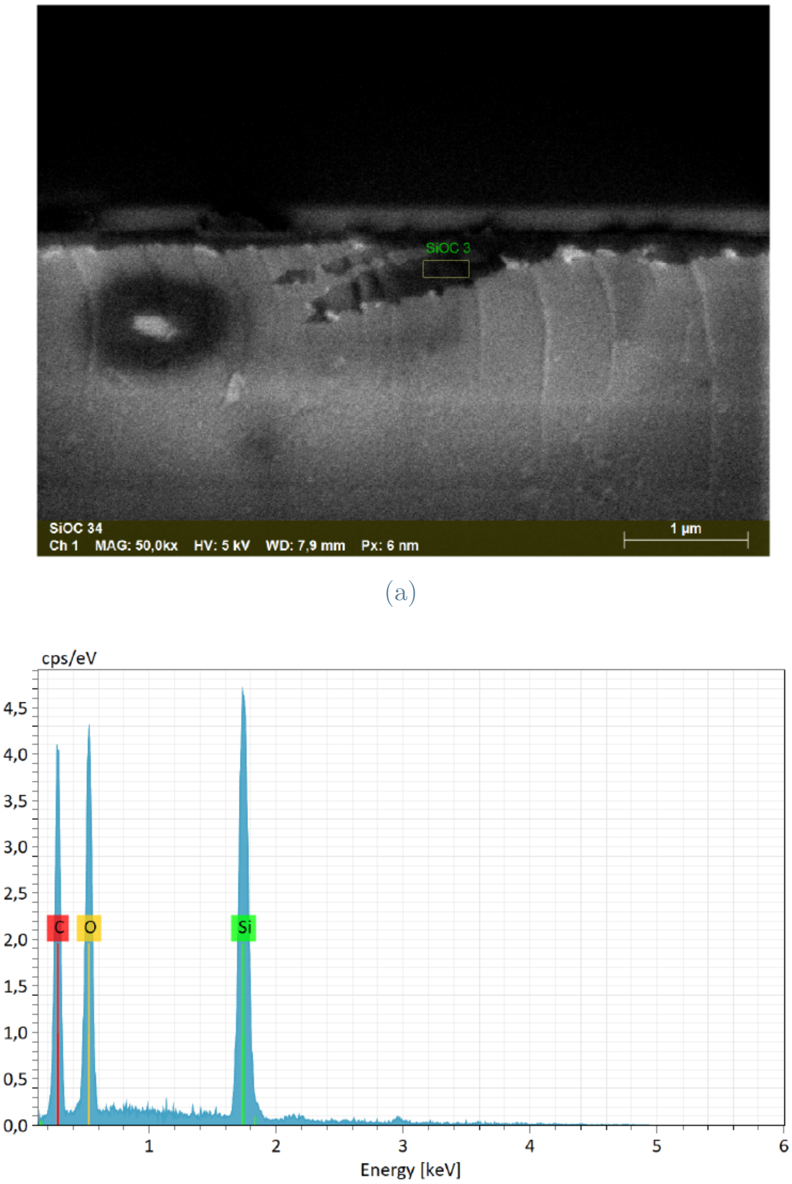

(a)

(b)

Figure 2.13: In (a) the area selected for the EDX analysis, while in (b) the peaks related to the quantity of element present in the thin film

Element	**Atomic n°**	**Mass %**	**Atom %**	**abs. error %**	**rel. error %**
Carbon	6	27.91	41.60	5.78	14.58
Oxygen	8	25.84	28.91	5.22	14.22
Silicon	14	46.26	29.49	3.18	4.84

Table 2.1: Compositional data of the SiOC with n = 2.25 from the EDX

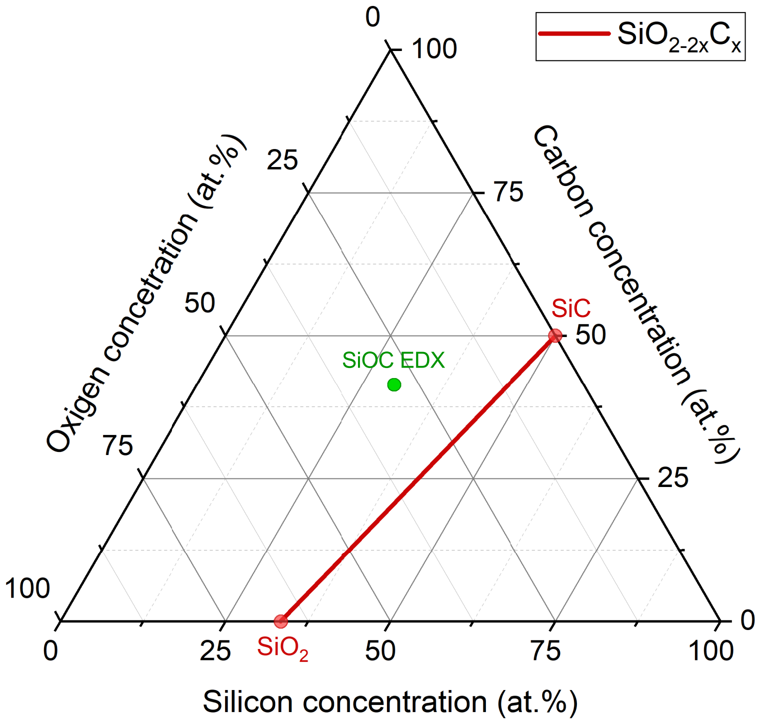

Figure 2.14: Ternary phase diagram for silicon oxycarbide with the composition obtained from the EDX. Although the value doesn't follow the line the absolute error of the system used is high, thus a more precise analysis such as the XPS and SIMS it's required to confirm and assess the chemical composition.

After that another EDX has been performed to see the composition along the thickness of the thin film to assess if there is a gradient also in the chemical structure of the film. A gradient in composition can lead to a gradient in the refractive index which in the sample is $\approx$ of 3%. Thus, after selecting the range of thickness to measure we obtain the results shown in Figure 2.15 and Figure 2.16. From the obtained data, it is not evident the presence of a gradient in the chemical composition, probably the gradient in the refractive index is not so big to justify it. Another EDX analysis with a thinner film could be more effective in the evaluation of a real chemical composition gradient.

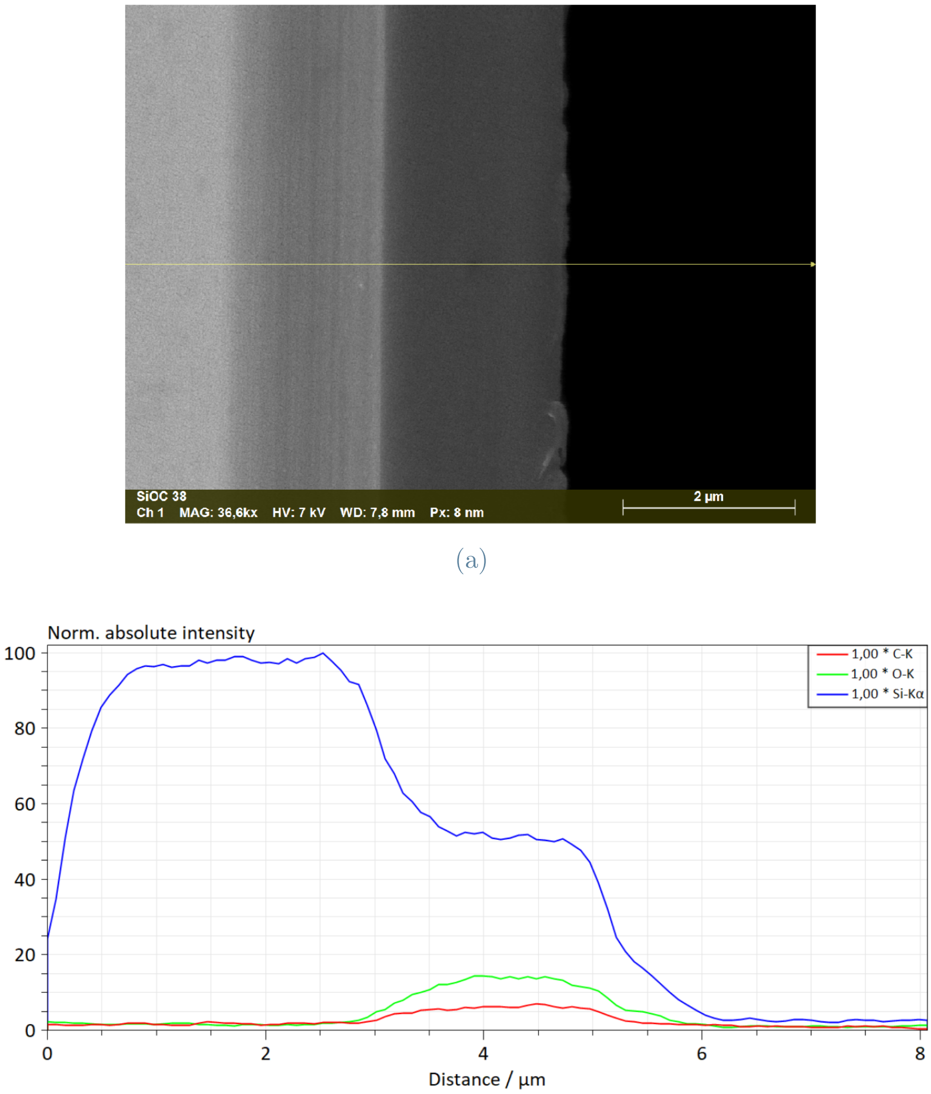

(a)

(b)

Figure 2.15: In (a) section used to analyze the composition along the thickness, while in (b) the elemental composition along the thickness (blue silicon, red carbon, green oxygen)

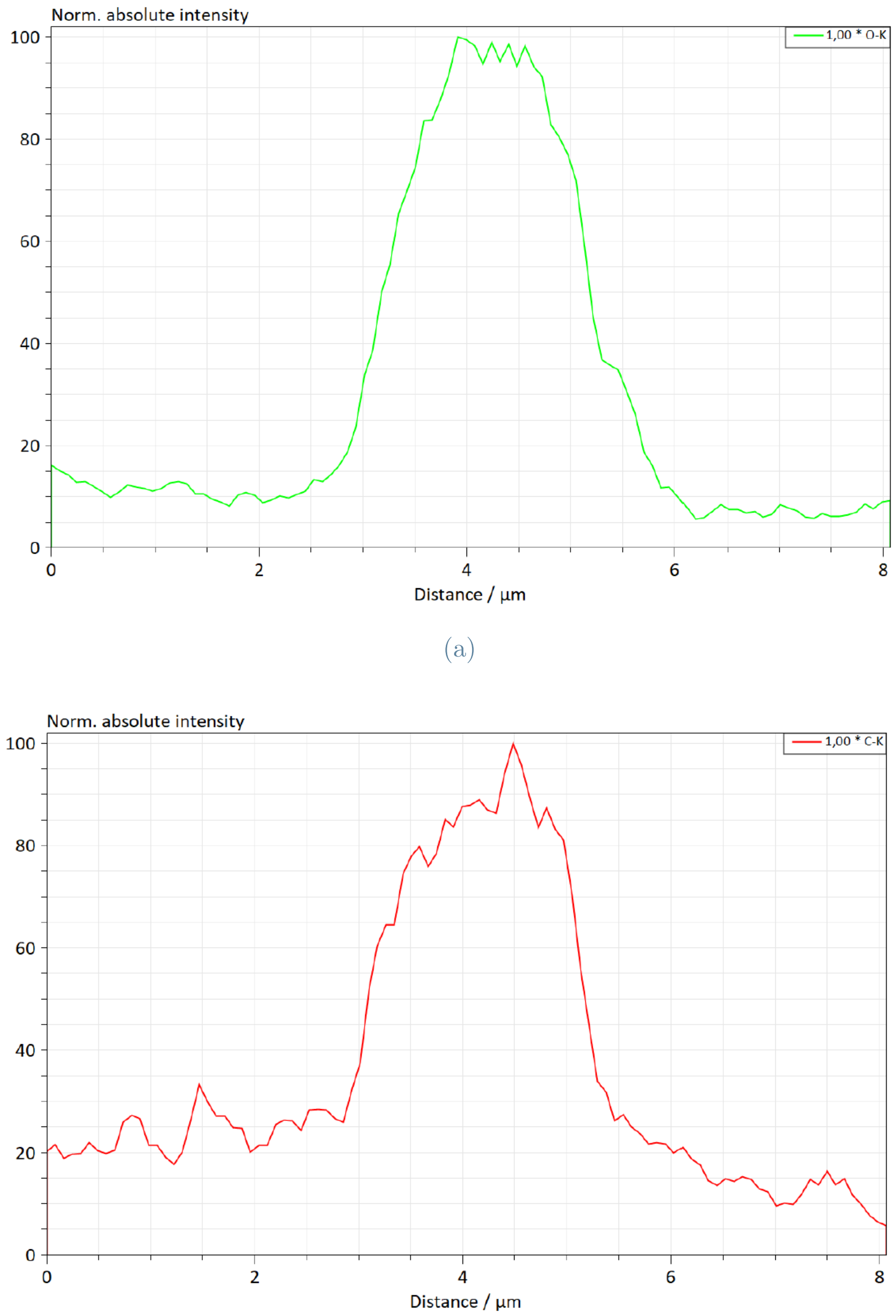

(a)

(b)

Figure 2.16: In (a) the composition of oxygen, while in (b) the composition of carbon

2.4. Process Optimization

To obtain a material with specific optical properties and to make the process reproducible it's important to understand which is the impact of the sputtering process parameters on them. For this reason, a study is performed in order to establish the best process for our purpose. In previous work [18] (Table 2.2) a general recipe to obtain a refractive index of 2.2 is used:

RF power (W)	**Ar flux (sccm)**	**O_2 flux (sccm)**	**Vacuum pressure (mbar)**	**Process pressure (mbar)**
280	10	0.7	10^{-6}	1.1×10^{-2}

Table 2.2: The recipe used in previous works to make SiOC with a refractive index of ≈ 2.2

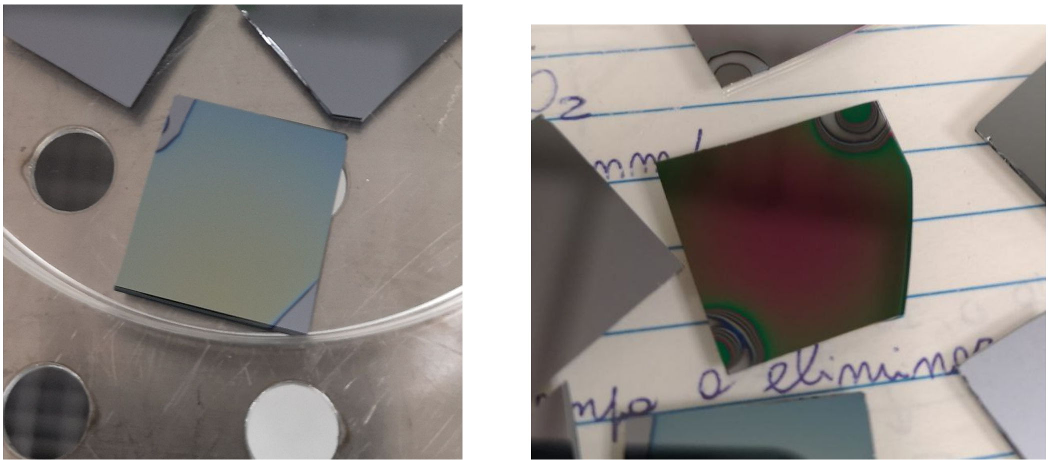
(a)
(b)

Figure 2.17: In Figure (a) 400 nm thin film of silicon oxide on silicon sample, while in (b) 550 nm thin film of silicon oxycarbide at 2.0.

Using the reported recipe the refractive index obtained results to be near the one of SiO_2 (1.5). This great change is due to the gate system valve for controlling the aperture of the turbo molecular pump, which was not present at the time of the previous experiments [35][18]. Adjusting the recipe by doubling the value of Ar flux we obtain a refractive index value of 2.0 (Figure 2.17). The presence and quantity of oxygen in the vacuum chamber play an important role in the reactive process for obtaining silicon oxycarbide. The amount of oxygen is primarily determined by the flux of O_2, but it can also be influenced by additional factors. For instance, atmospheric humidity can affect the oxygen levels in the chamber [31]. Furthermore, oxygen absorption on the internal surfaces [27] of the vacuum chamber can impact the overall quantity of oxygen. Therefore, careful consideration and control of these factors are important to ensure the desired oxygen concentration for the successful synthesis of silicon oxycarbide films. More oxygen is present in the chamber and lower will be the film's refractive index. A systematic approach was adopted to obtain SiOC film with expected characteristics. The approach consists in modifying the sputtering parameters one by one while keeping the others constant. By following this approach, it becomes possible to establish correlations among the obtained results. Each test must be performed in separate sessions for better tracking and analysis of experimental parameters, deposition conditions, and resulting film properties. The primary focus was on analyzing the changes in the refractive indexes of the films, as they provide valuable insights into the material properties. As a result of these parameter adjustments, some linear behaviors were observed in the refractive index values. Thus, as shown in Figure 2.18 a lot of samples have been made. The extinction coefficient is also obtained from ellipsometry analysis, but because of the very low values in IR range, the measurements may not be so reliable. This is caused by the measurement limitations of the ellipsometer system.

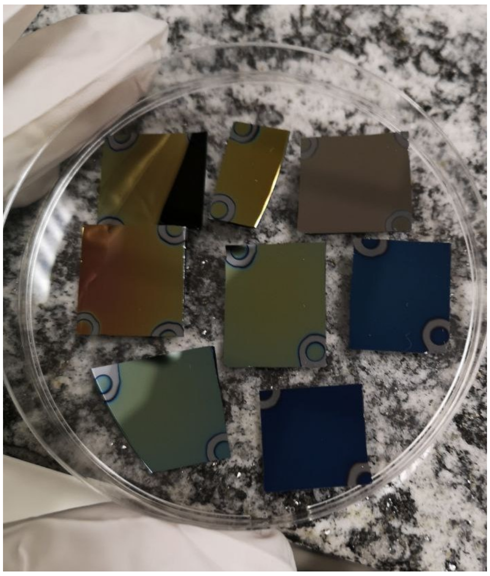

Figure 2.18: SiOC with different refractive indexes: from right to left the refractive index is higher. On top right a thin film of silicon carbide

2.4.1. Oxygen flux ratio dependence

In this section is shown the O_2 ratio dependence changing the Ar flux. Changing the Ar flux instead of O_2 is desirable because the refractive index value change strongly with a little variation of oxygen. Moreover increasing too much the oxygen flow can induce a hysteresis loop [24] while instead of decreasing it too much it's possible to reach the sputtering system limit (fixed at 0.5 sccm). The O_2 ratio is calculated by taking the O_2 flux and dividing it by the total flux in the chamber (the sum of Ar and O_2 fluxes).

All the samples analyzed in this case are produced under the same vacuum and process pressure conditions, 3.2×10^{-6} mbar and 1.1×10^{-2} mbar, respectively. The RF power used for the deposition process is also kept constant at 280 W. As an approximation, the quantity of oxygen in the chamber can be found considering the partial pressures of the gases. In order to determine the oxygen partial pressure in the process, the O_2 flow ratio needs to be multiplied by the process pressure. By multiplying the O_2 flow ratio by the process pressure, the oxygen partial pressure can be calculated. To obtain the trend on how the O_2 flux ratio changes the optical properties we made three samples as reported in Table 2.3.

Sample	**Ar flux (sccm)**	**O_2 flux (sccm)**	**O_2 ratio**	**Refractive index (at 1550 nm)**	**Extinction coefficient (at 1550 nm)**
1	20	0.7	0.0338	1.846	1.530×10^{-4}
2	25	0.7	0.0272	2.044	2.633×10^{-4}
3	30	0.7	0.0228	2.112	9.217×10^{-4}

Table 2.3: Data of three samples with different O_2 flux ratio

In Figure 2.19a, the plot displays the refractive indexes as a function of wavelength for different oxygen content. It is evident that there is a significant change in the refractive index values across the different oxygen concentrations. If we take values of refractive index at a specific wavelength, such as 1550 nm, a linear response can be observed as depicted in Figure 2.19b. Figure 2.20 illustrates the variation of the extinction coefficient. It is observed that the values exhibit significant changes in the infrared (IR) spectra. At the same time, in the visible region, the curves tend to converge, suggesting a reduced sensitivity to the oxygen concentration in this range.

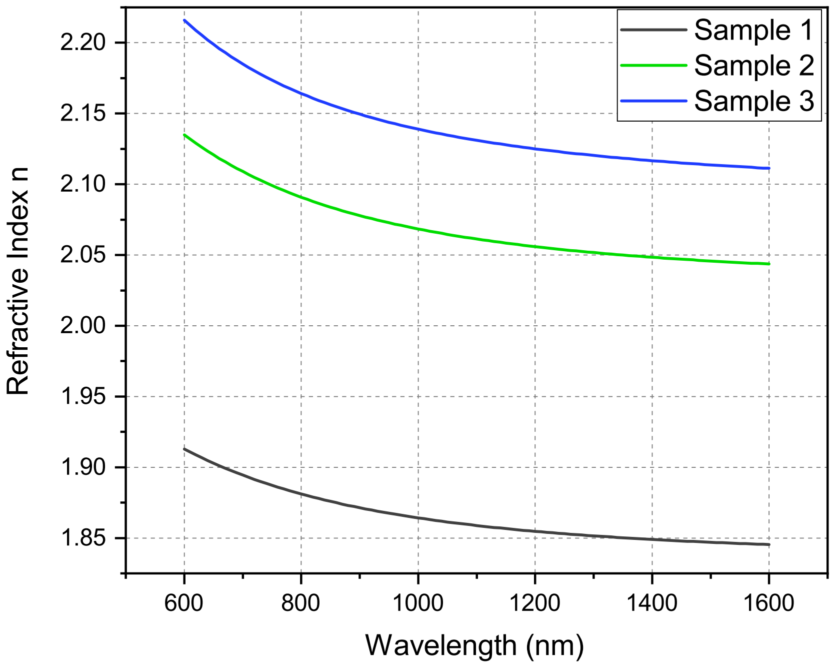

(a)

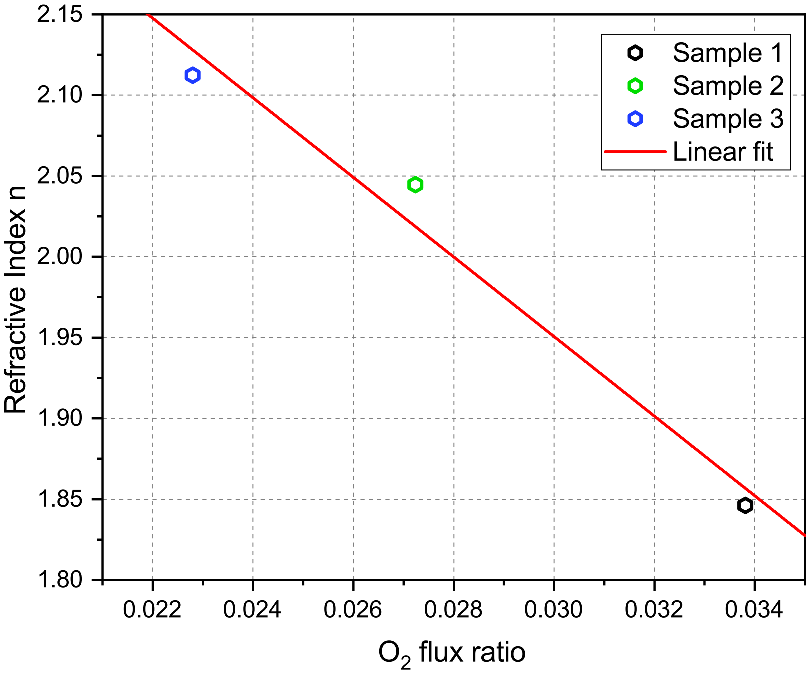

(b)

Figure 2.19: In (a) different refractive index trend changing the oxygen flux ratio while in (b) the linear fit the refractive indexes taken at 1550 nm

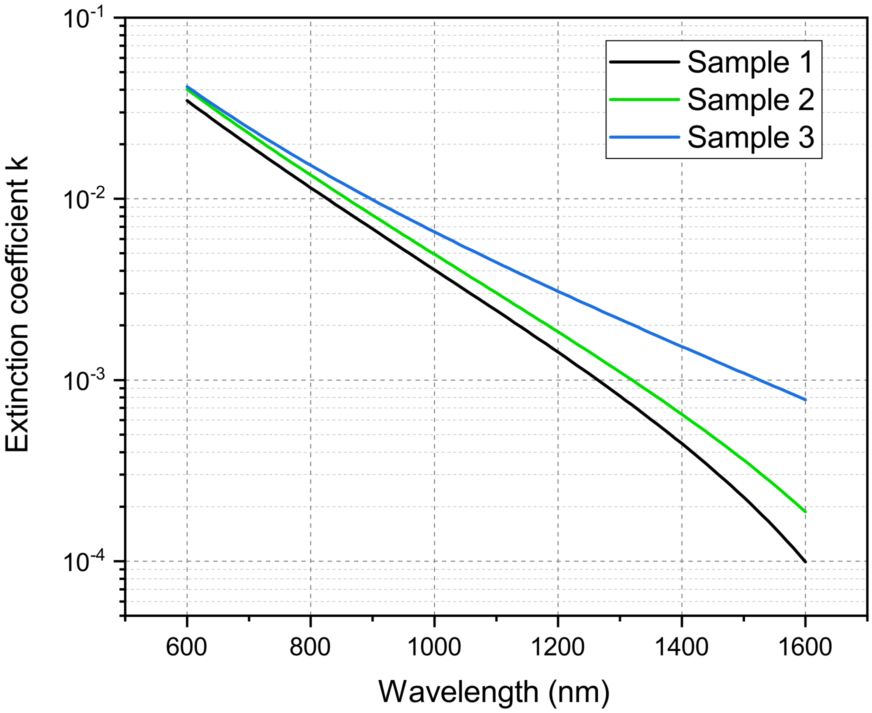

Figure 2.20: Extinction coefficients trends in semi-logarithm scale

2.4.2. Vacuum pressure dependence

The vacuum pressure is the pressure reached by the chamber before the sputtering process. This parameter has a high influence on the refractive index because water is a contaminant. To obtain the trend on how the vacuum pressure changes the optical properties, we made three samples as reported in Table 2.4. For all the samples analyzed in this case, a constant Ar flux of 30 sccm, O_2 flux of 0.7 sccm, process pressure of 1.1×10^{-2} mbar, and RF power of 280 W is maintained.

Sample	**Vacuum pressure (mbar)**	**Refractive index (1550 nm)**	**Extinction coefficient (1550 nm)**
4	5×10^{-6}	2.040	-
5	3.2×10^{-6}	2.112	9.217×10^{-4}
6	6.2×10^{-7}	2.213	-

Table 2.4: Data of three samples with different vacuum pressure

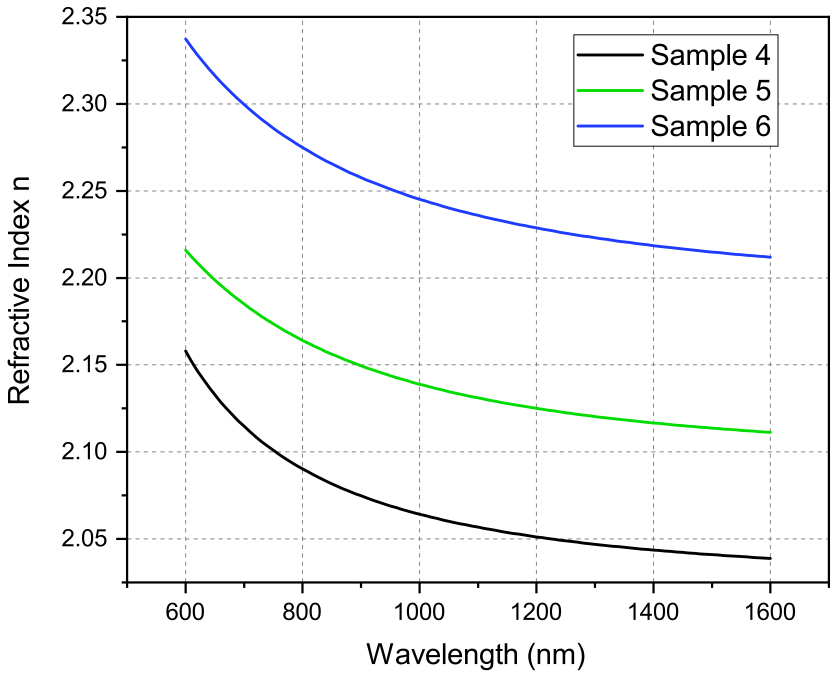

(a)

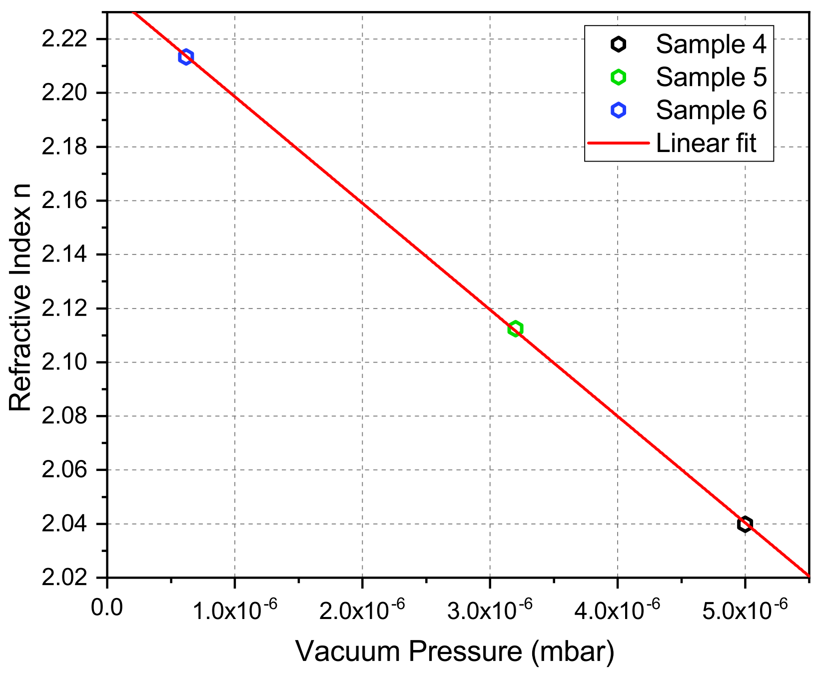

(b)

Figure 2.21: In (a)the refractive indexes trend with different vacuum pressures, while in (b) the liner fit of three different refractive indexes taken at 1550 nm

In Figure 2.21a, the plot demonstrates that the vacuum pressure has an impact on the film properties similar to the one of the oxygen content. Moreover, in Figure 2.21b, a linear fit is obtained, providing evidence for the dependence of the water content in the vacuum chamber. The H_2O can be found on every surface because of the atmospheric humidity and act as an oxidizing agent [36]. These controlled conditions allowed for a direct comparison of the effects of vacuum pressure and water content on the observed film properties. The optimal pressure range for achieving the best results in the deposition process is typically below 10^{-6} mbar. However, reaching such ultra-high vacuum levels can be time-consuming. Therefore, in one session a practical approach is to aim for the lowest vacuum pressure attainable while simultaneously adjusting the quantity of oxygen in the chamber. The extinction coefficients are also reported here, but in two cases the values are so small that the ellipsometer system gives us 0 for the entire IR range.

2.4.3. RF power dependence and Deposition rates

In accordance with the previous work [18], it is settled that the refractive index is also influenced by the RF power. In order to further investigate this relationship, we carried out experiments to examine the dependence of the refractive index on RF power while keeping the gas flows constantly at 30 sccm for Argon and 0.7 sccm for Oxygen, as well as maintaining consistent vacuum and process pressure (respectively 3.2×10^{-6} and 1.1×10^{-2} mbar). To obtain the trend on how the RF power changes the optical properties and the deposition rates we made three samples as reported in Table 2.5.

Sample	**RF power (W)**	**Refractive index (1550 nm)**	**Deposition rates (nm/min)**
7	160	1.57627	20.8639
8	220	2.03238	26.7816
9	280	2.31366	31.9270

Table 2.5: Data of three samples with different RF powers

In Figure 2.22a, the influence of RF power on the refractive index is evident and consistent with previous research findings [35]. However, in Figure 2.22b, the deposition rates show different results, particularly at low RF power.

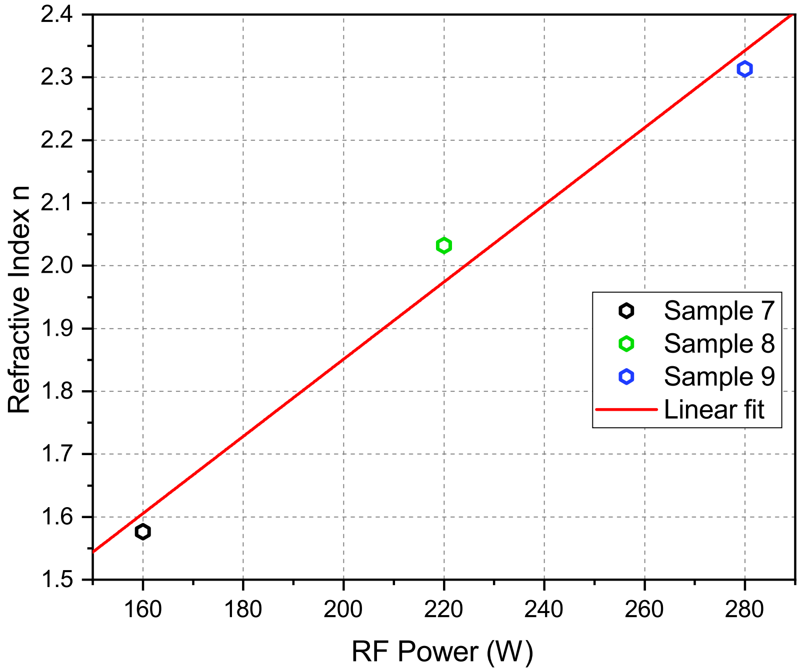

(a)

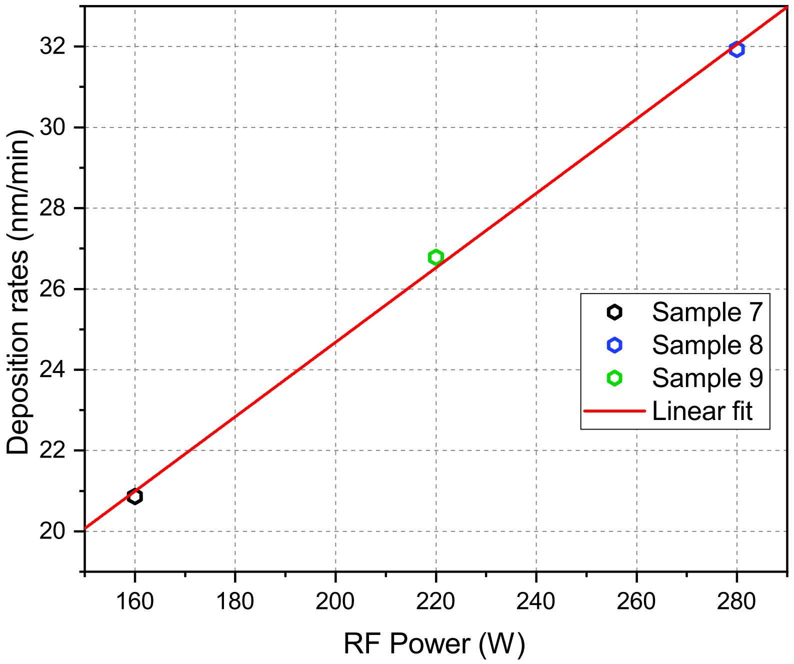

(b)

Figure 2.22: In (a) the linear fit of three different refractive indexes taken at 1550 nm, while in (b) the linear fit of the deposition rates based on the thickness of the thin films obtained

The observed changes from the expected trend can be attributed to the different quantities of oxygen present in the vacuum chamber during the deposition process. The reactive gas content plays a significant role in the reaction dynamics and can impact the growth rate of the thin films [17]. Therefore, it is probable that the different oxygen levels at low RF power settings may lead to variations in the deposition rates. Further investigations and adjustments in the oxygen quantity control may help to address this difference and achieve more consistent deposition rates across different RF power levels.

2.4.4. Conclusion

Based on the data obtained, we have identified several key factors for achieving a silicon oxycarbide thin film with a refractive index higher than 2.0 and a fast sputtering process. These factors include:

- Decreasing the vacuum pressure as much as possible
- Decreasing the oxygen flux ratio
- Increasing the RF power as much as possible

By optimizing the parameters of vacuum pressure, oxygen flux ratio, and RF power, it is possible to obtain a silicon oxycarbide thin film with a refractive index close to the desired value of 2.2. In this work, a general recipe was developed to produce a thin film with optical properties that closely match the desired specifications and it is shown in Table 2.6. However, it is important to note that the reproducibility and reliability of the results may vary, and adjustments may need to be made. To implement the optimal process flow, it is recommended to initially make a thin film using the general recipe provided. The resulting film can then be analyzed using the ellipsometer to determine its optical properties. Based on the analysis, the process parameters can be adjusted accordingly for a second thin film deposition to fine-tune the film's optical properties and achieve the desired refractive index.

RF power (W)	**Ar flux (sccm)**	**O_2 flux (sccm)**	**Vacuum pressure (mbar)**	**Process pressure (mbar)**
280	30	0.7	10^{-6}	1.1×10^{-2}

Table 2.6: General recipe to obtain the silicon oxycarbide with the desired optical properties

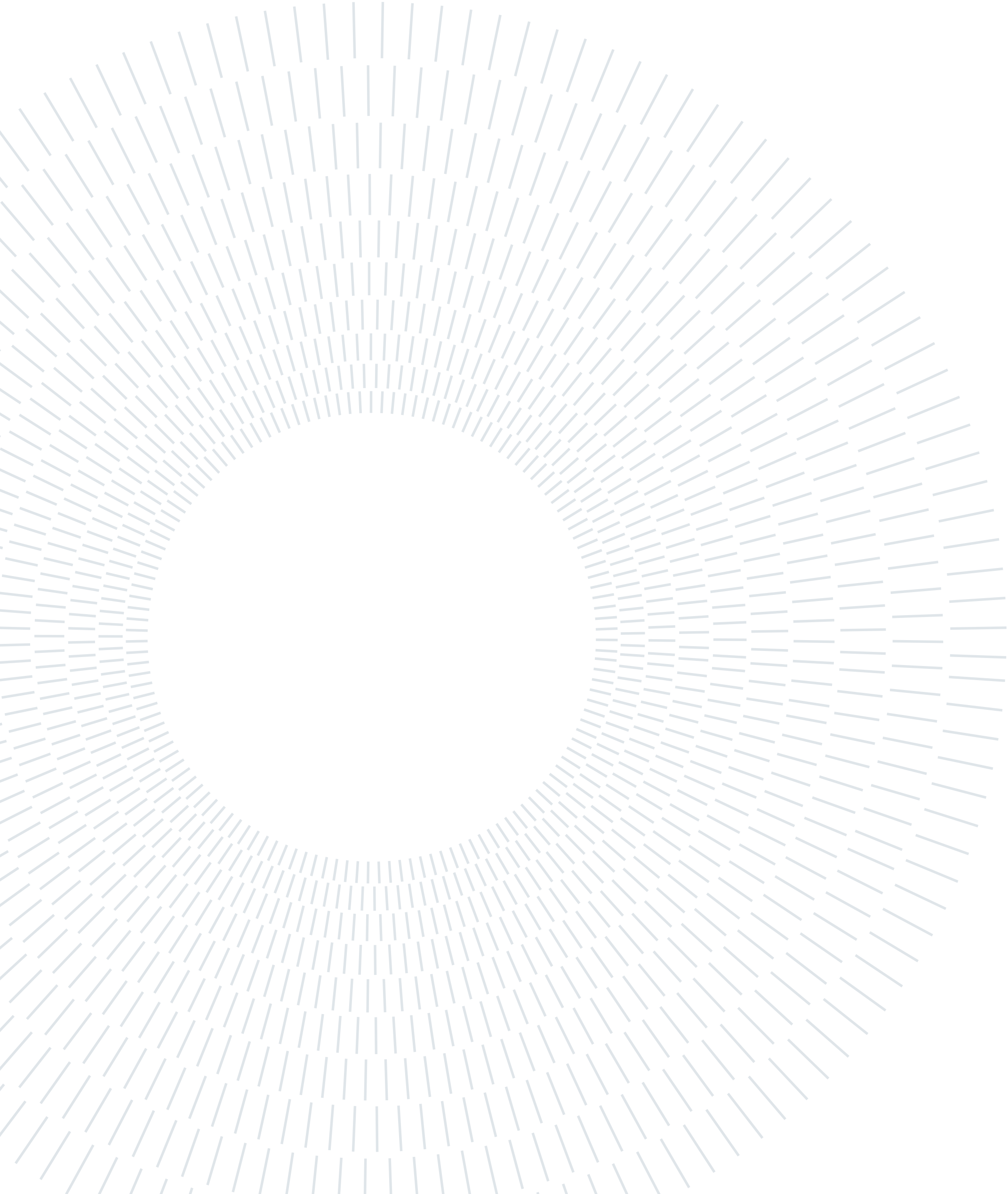

3 | SiOC integration on chip

3.1. Silicon nitride platform description

The integration of silicon oxycarbide in an integrated photonic platform is really promising to exploit the high thermo-optic coefficient for efficient thermal actuator applications. The presence of SiOC on a waveguide changes the propagation of the confined electromagnetic wave which will have different properties. Starting with the layout of the chip, as depicted in Figure 3.2a, it is composed of 13 offset waveguides and all of them have dimensions of 330 nm thick and 1.5 μm in width. Each waveguide differs in length, starting from 0.29 cm to 0.89 with an incremental unit change of 0.05. As shown in Figure (Figure 3.1a) the chip is composed of a silicon nitride core, a silicon oxide substrate, and a polymer photoresist (the SU8) as cladding. On the chip, there are some window zones where the waveguides are not covered by the cladding (as shown in Figure 3.1b). During the sputtering deposition, the silicon oxycarbide will cover the window zones, so it will be in direct contact with the Si_3N_4 waveguide making a hybrid waveguide.

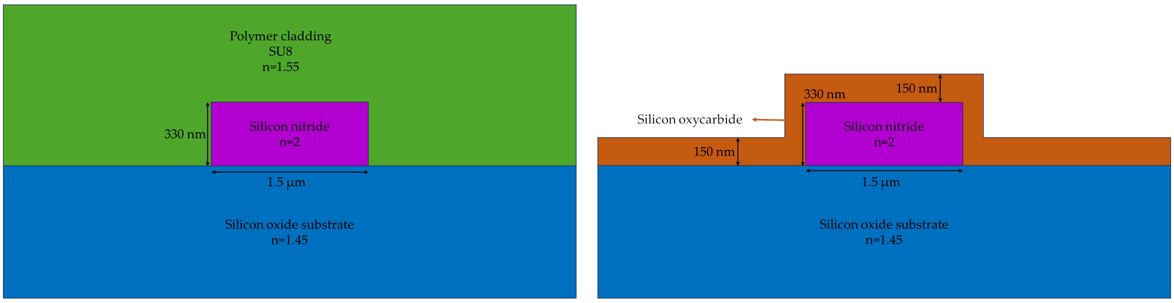

(a)

(b)

Figure 3.1: In (a) a simple scheme of the cross-section of the waveguide with the cladding on top while in (b) a simple scheme of a cross-section of the waveguide in the window zone with SiOC on top

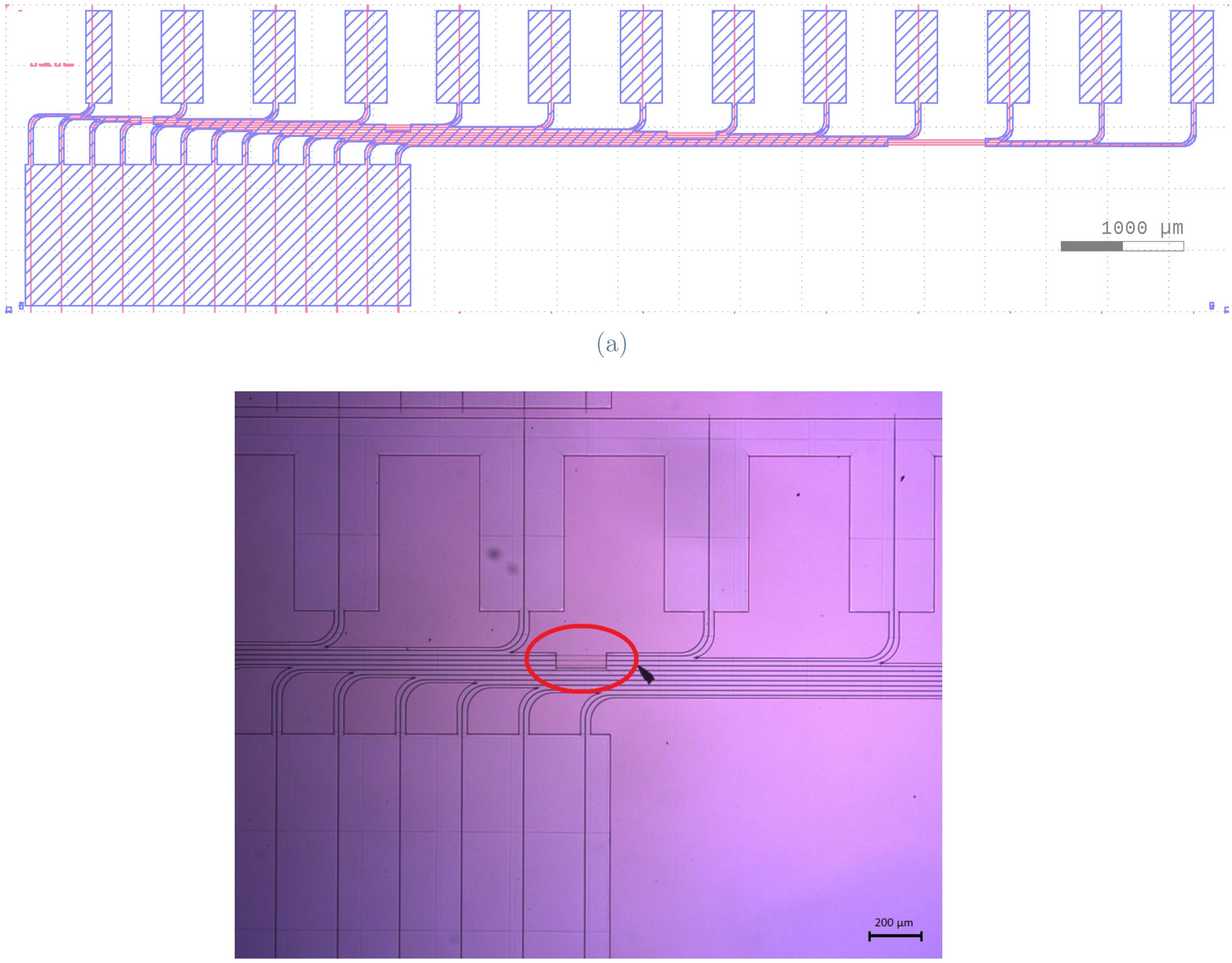

(a)

(b)

Figure 3.2: In (a) the layout of the chip from KLayout, the red lines represent the waveguides, while the blue boxes the cladding. In (b) a magnification of a real chip with the window where the waveguides are not covered by the cladding.

3.1.1. EM simulations

To design our silicon oxycarbide thermal actuator we leverage electromagnetic simulations from the software Lumerical developed by Ansys. It allows us to calculate all the most essential properties of a waveguide like the modal effective index n_{eff}, propagation losses, and the guided electric field intensity distribution through FDE simulations. The wavelength used for our experiments is equal to 1550 nm which is a standard in the telecommunication background. The EM field in a waveguide develops creating modes that are fundamental for the transmission of signals in telecommunication. In our work we analyze the fundamental transverse electric (TE) mode and how it changes. The SiOC will be deposited on the silicon nitride waveguide of the window zones and the structure formed becomes the core (Figure 3.3a) for the modes allowing the change of all the properties of the electromagnetic fields. The electric field intensity distribution of the mode is depicted in Figure 3.3b

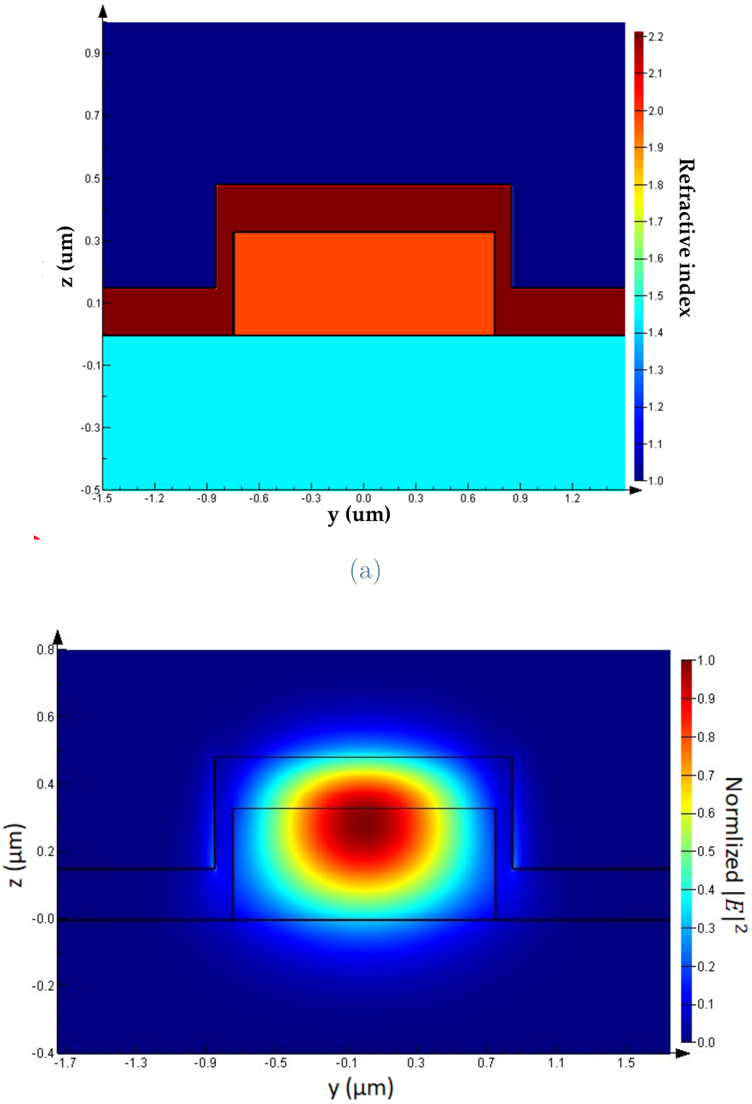

(a)

(b)

Figure 3.3: In (a) The shape of the first TE mode in the window cross-section. The mode is overlapped with the SiOC layer. In (b) the material refractive index (red SiOC, orange Si_3N_4, light blue SiO_2

The silicon oxycarbide used for the simulation has a refractive index at 1550 nm of 2.21 and an extinction coefficient of 0.0036. Due to the fact that SiOC has a higher refractive index with respect to silicon nitride, there will be an overlap with the SiOC layer. We calculated that with a thickness of 150 nm, the overlap with the SiOC layer is high enough

(≈ 25%) to allow a strong modification of the characteristics of the mode in the waveguide.

3.2. Fabrication process

From the previous section, we want to fabricate what we simulated which is to deposit the SiOC on the waveguides. We start with uncladded silicon nitride waveguides fabricated from AMO cleanroom at the University of Aachen. For the cladding, we choose to use a polymer because of the great versatility of the material. We start with the lithography process holds a fundamental role in generating an appropriate pattern for the cladding on the microchip. In the following section, all the procedures involved in producing the polymer cladding will be reported.

The using of a polymer as a waveguide cladding needs the presence of specific desirable characteristics, including robust adhesion to the substrate, high sensitivity, resilience against both wet and dry etching, simple processing, high purity, prolonged shelf life, minimal solvent demands, cost-effectiveness, and a high glass transition temperature (T_g) [22]. For the specific application at hand, the chosen polymer is SU8-2000, an epoxy-based negative photoresist. SU8-2000 has been selected due to its suitability for permanent applications, wherein it is imaged, cured, and retained on the device [21]. This particular photoresist, SU8-2000, exhibits a range of desirable characteristics that align with our requirements. These include high thermal and chemical resistance, and the capacity to absorb UV light within a wavelength range compatible with our lithography machine.

Selected the cladding material we have to deposit it onto the chip. Spin-coating is a standard method for depositing thin films of photoresist, such as SU8-2000. This process involves clamping the sample onto a vacuum chuck, where some milliliter of the polymer photoresist is placed at the center of the sample and then it is rapidly rotated at high speed. The even spreading of the photoresist across the sample surface is due to the centrifugal force generated by the rotation, resulting in a consistent coating. Moreover, during the spinning process, the air is pumped outwardly along the surface of the wafer, which assists in the drying and curing of the photoresist coating [8]. The rotation speed is based on the material and its thickness. The thickness of cladding is chosen by how much the electric field intensity distribution decay in the SU8. Thus, we choose 4 μm of cladding because the intensity of the electric field at this thickness is negligible, therefore the rotation speed is set to 4000 RPM [21]. All the steps for the spin-coating process are resumed in Figure 3.4. In conclusion, the act of spin-coating is a highly effective and extensively used method for producing uniform and high-quality thin films of photoresist on flat surfaces.

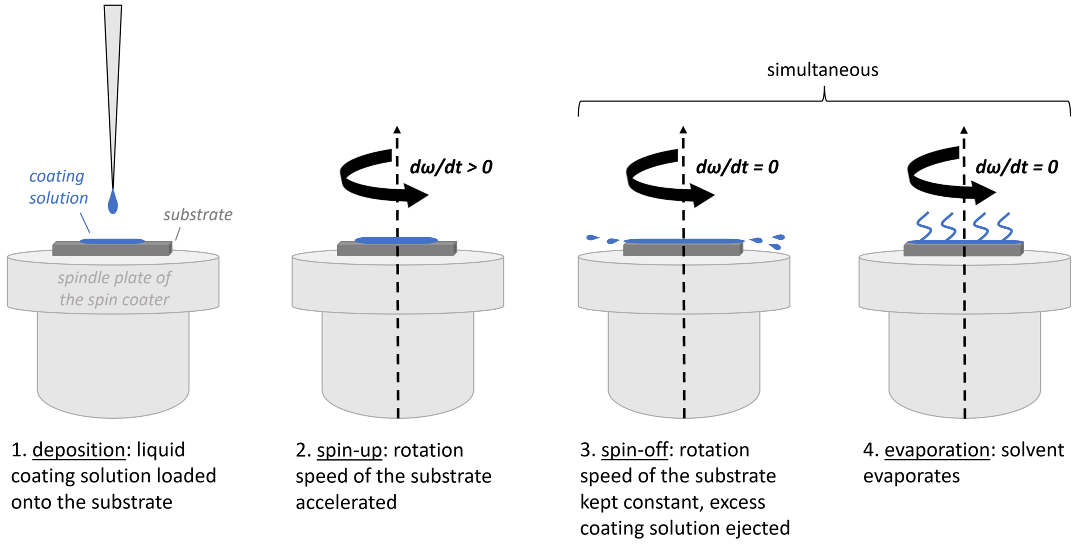

Figure 3.4: Spincoating processes step-by-step [4]

Applied the photoresist, it is necessary to carry out a specific curing process in order to harden the polymer and eliminate all traces of the solvent (as the photoresist can have an amount of solvent ranging from 4-10% [22]). The process of soft-bake plays a fundamental role in improving the adhesion of the photoresist to the substrate and reducing the amount of internal stress present. Appropriate time and temperature settings are needed for the soft-bake (in Table 3.1).

Finished the soft-bake process, the UV exposure process needs for the polymer cross-linking to begin. The cross-linking of SU8 takes place within the UV range of 350-400 nm and requires a specific dose that is determined by dividing the light intensity by the exposure time (the recommended dose for 4 μm of SU8 cross-linking is 90-105 J/cm^2 [21]). In our configuration, the lithography system is used because it has integrated a UV diode of 365 nm of wavelength necessary for cross-linking.

Lithography is the process of transferring a pattern into a reactive polymer film (termed a photoresist) which will subsequently be used to replicate that pattern into an underlying thin film or conductor [33]. In our work, the Heidelberg MLA100 was utilized for the patterning process on the photonic chip. The Heidelberg MLA100 (Figure 3.5) is an optical lithography system designed specifically for direct writing on photoresists without the need for a photomask. Its optical system enables the fabrication of structures as small as 1 μm with a high speed of 50 mm^2/min.

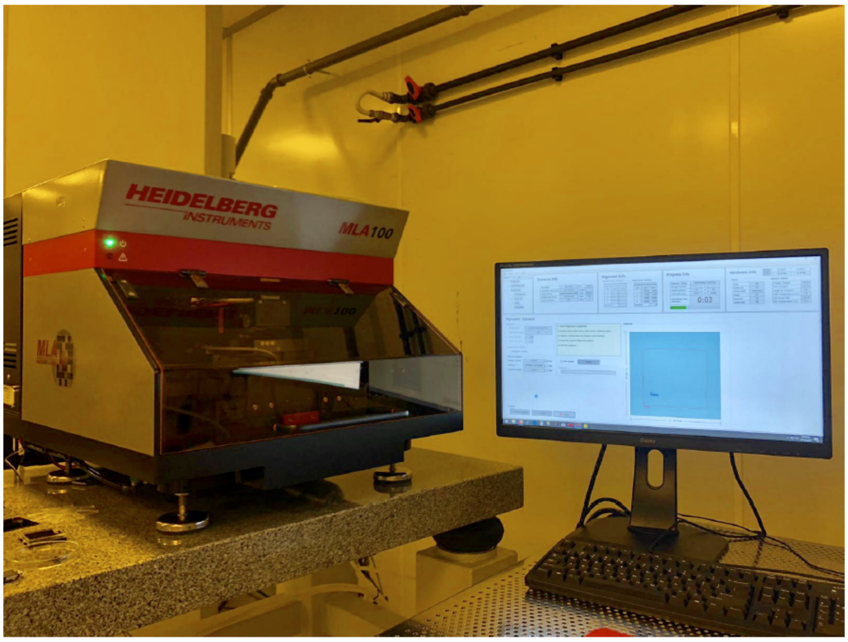

Figure 3.5: Lithographic system Heidelberg MLA100

Following the UV exposure, a post-exposure bake is required to ensure the fulfillment of the crosslinking of the polymer and facilitate the evaporation of any remaining solvent. Once this step has been completed, the developing process begins in order to eliminate the unpatterned photoresist. To finalize this process, the chip is immersed in a SU8 developer solution for one minute, rinse in IPA to remove all the traces of the developer, and dried gently with a nitrogen gas gun.

If the photoresist is used for temperature applications a hard baking process or a higher mechanical resistance is wanted [21] a hard-bake step is conducted to eliminate any residual casting solvents and anneal the resist film. This step addresses any weaknesses in the resist film caused by developer penetration along the resist-substrate interface or resists swelling. The temperature and duration of the hard bake are critical to the success of the process. In brief, the fabrication process entails a sequence of crucial stages that require precision. In Table 3.1 all the times and temperatures of the baking processes are reported, while in Figure 3.6 is resumed all the steps of curing.

Step	Baking temperature (°C)	Baking time (min)
Soft bake	95	1
Post-exposure bake	95	2
Hard bake	150	7

Table 3.1: All the baking step with temperatures and times used for curing the photoresist

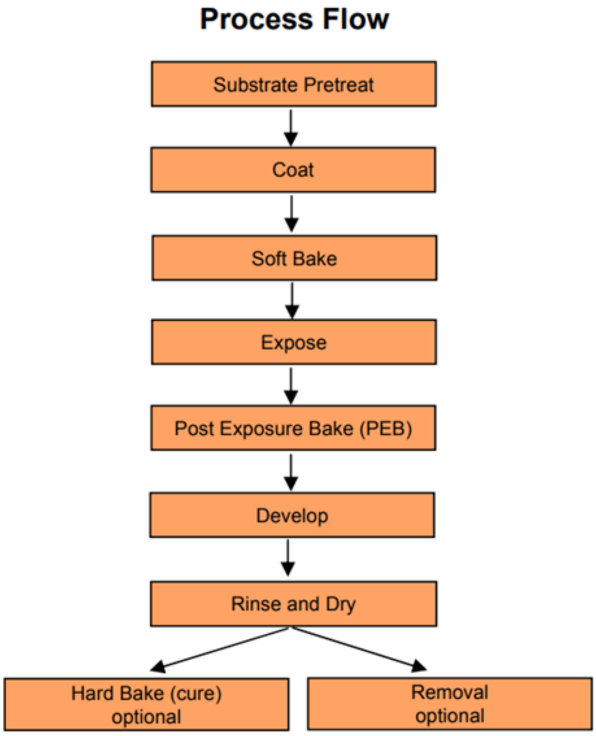

Figure 3.6: Process flow for the curing processes adapted from [21]. In our work the hard-bake step is mandatory to evaporate all the solvent

The chip must be diced into smaller sections. To ensure the chip's safety and prevent any possible damage, a polymer protective coating is employed during this process (Figure 3.7). The protective coating is deposited through a spin-coating process. Once the protective coating is appropriately applied, the chip is secured onto a dicing saw and meticulously divided into chips.

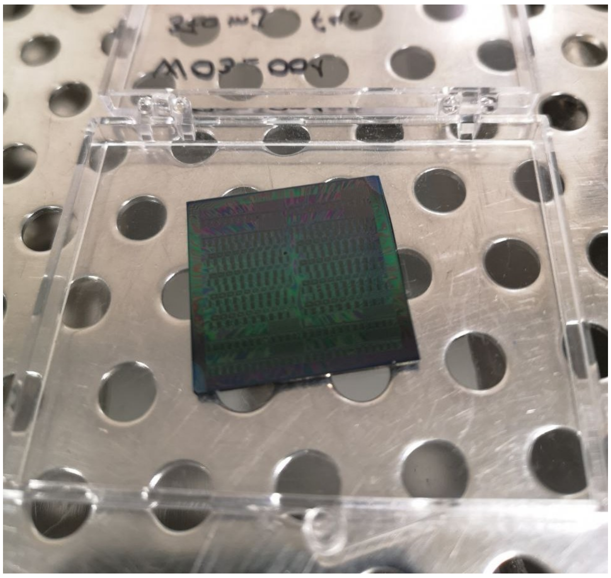

Figure 3.7: Chip without bubbles with a protective coating on top

3.3. Process optimization

Now we describe all the optimization of integrating a sputtering process to deposit a layer upon a polymer cladding. Phenomena such as polymeric outgassing, polymeric temperature limit, and substrate thermal management as well as the consequences during the deposition have been analyzed.

3.3.1. Temperature

In general, polymers cannot sustain too high temperatures. This is because of their thermal degradation in which the polymeric chains will dissociate in elemental particles like CO_2, H_2O, or some other chemicals. The same occurs also for the SU8 which starts to lose weight at 200°C and becomes relevant at temperatures over than 350°C (Figure 3.8). In the sputtering system, the increase of temperature on the target is expected, and a cooling system is present but for the substrate is not. For this reason, we investigated the variation of temperature in time with different RF power of the sputtering system. To measure the temperature of the substrate during the deposition process we used a thermocouple fixed with a metal clamp directly on the center of the metal holder.

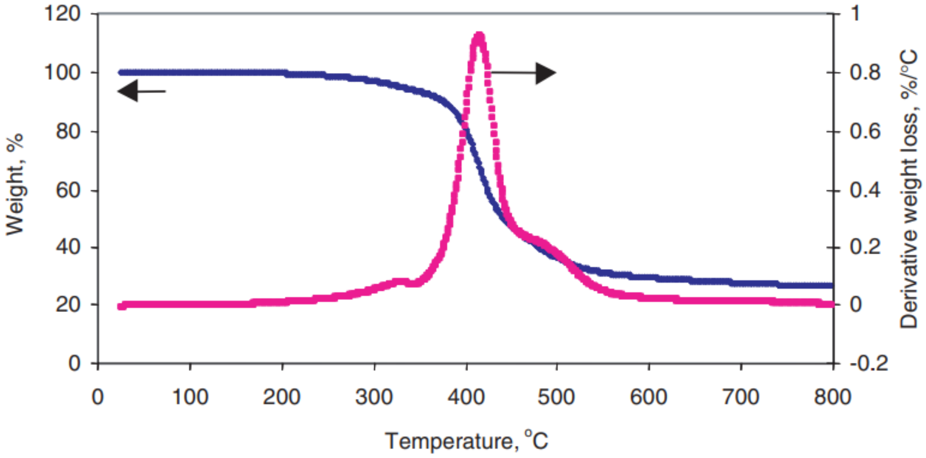

(a)

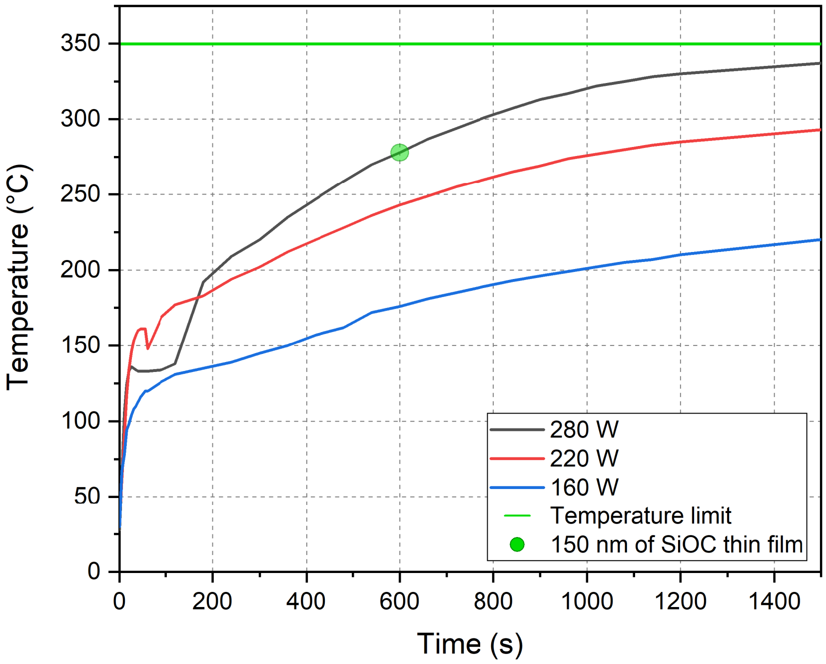

(b)

Figure 3.8: In (a) the weight loss of the SU8 with 5 minutes of pre-bake and 15 minutes of hard bake [9]. In (b) the temperature variation of different RF power on the substrate during the sputtering deposition with the

At a certain time and RF power, the temperature of the substrate can overcome the temperature limit. The most favorable condition for the polymer (as shown in Figure 3.8b) is to work at 160 W, but to obtain the silicon oxycarbide with the highest refractive index it is better to work at 280 W. Considering the thickness of the thin film needed for our application (150 nm) and the time to obtain it at 280 W (5 minutes) the polymer should resist. If a larger thickness is required it would be better to work at lower RF power to avoid any material weight losses. The temperature may cause a severe outgassing of the polymer. In particular, the polymer decomposes in CO_2 and this can cause a variation of the optical constant of the thin film during the deposition [9]. But analyzing the thin we put with the chip sample the refractive index didn't change so much with respect to the general recipe. Thus, in our case, the outgassing is not relevant.

3.3.2. Thermal management

The chip patterned is put in the sputtering system and the SiOC deposition process has been made. But on the chip appears several bubbles where the cladding area is bigger (as shown in Figure 3.9). To solve this problem we investigate the reasons behind this behavior. The substrate for our waveguides is a 2.8 μm layer of SiO_2 situated atop 500 μm silicon. SiO_2 acts as a thermal insulator, potentially hindering the proper curing of the photoresist, solvent evaporation, and heat transmission during the deposition process. Thus, the thermal conductivity of the substrate is a perfect candidate to test how much affects the lithography steps to make the cladding. Therefore, we conducted tests on three different substrates with different thermal conductivities, namely silica glass, borosilicate glass, and silicon (their thermal conductivities are summarized in Table 3.2). Each substrate underwent a cleaning process, SU8 deposition, and sputtering.

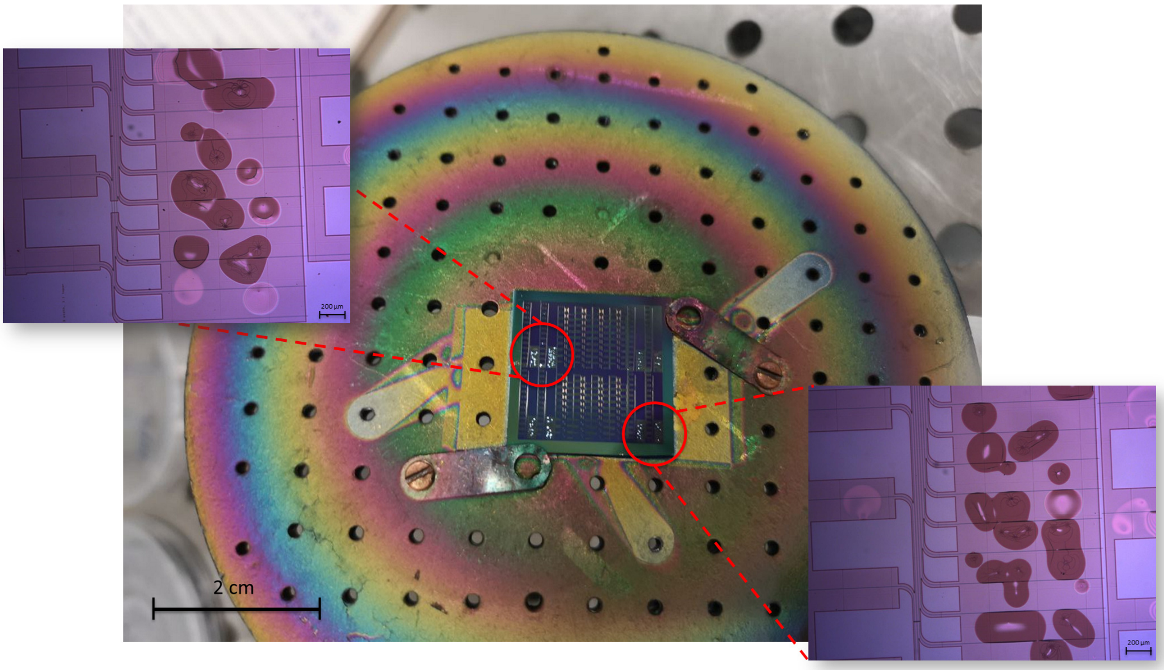

Figure 3.9: The photonic chip after the sputtering deposition, with microscope images of the bubbles on the chip cladding

Material	**Thermal conductivity** ($W/m \cdot K$)
SiO_2 glass	0.8-0.93[28]
Boron-silicate glass	1.1-1.93[28]
Silicon	3.8[32]

Table 3.2: Thermal conductivities data of the materials we used in the experiments

We try with a silica glass substrate microscope slide with a thickness of 1 mm, and it is evident that the SU8 material was not completely cured during the baking process, resulting in inadequate heat for solvent evaporation and the formation of many bubbles as shown in Figure 3.10. Certainly, also the thickness of the substrate has its influence, so for the following, we use materials with lower values of it.

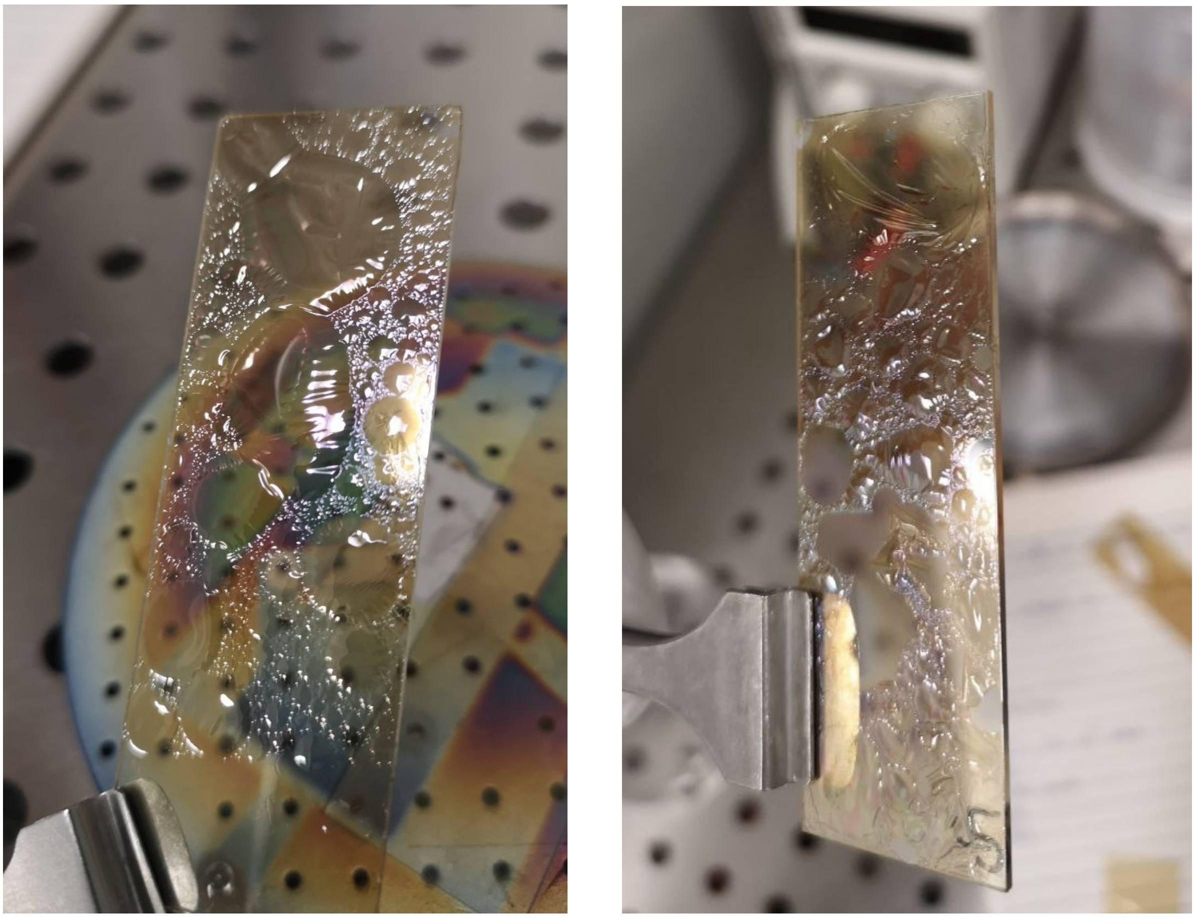
(a) (b)

Figure 3.10: In (a) the SU8 not hard-baked on a silica microscope slide (3x1 inches), while in (b) the SU8 hard-baked on a silica microscope slide.

For a boron-silicate glass, 0.5 mm thick and with better thermal conductivity and smaller thickness, smaller bubbles are observed (Figure 3.11). This observation highlights the significance of both the thickness and thermal conductivity of the substrate material.

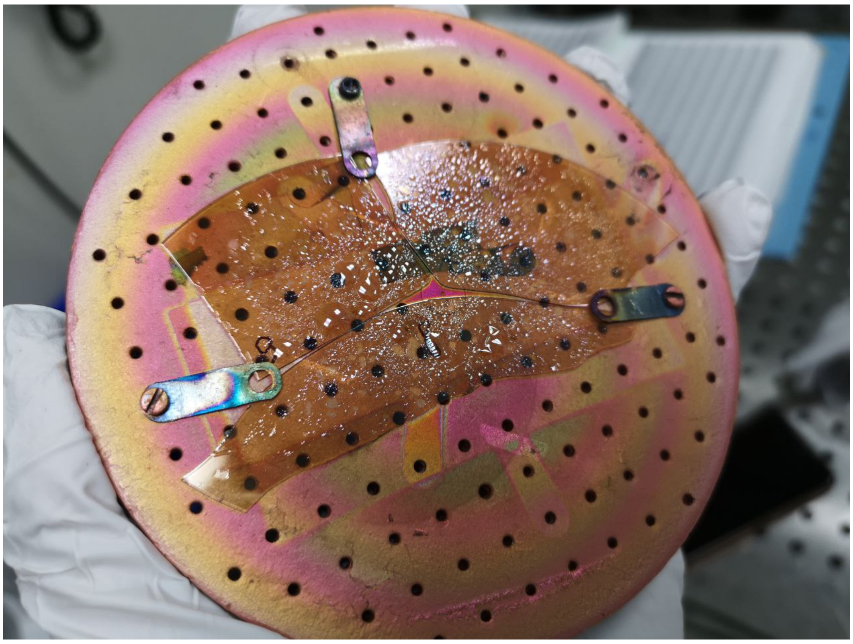

Figure 3.11: SU8 on boron-silicate glass disc after the sputtering process

On silicon, we can notice that the also hard-bake has a great influence in removing all the traces of solvent. Bubbles appear when the solvent has not yet evaporated Thus, if we make a hard-bake process after the development of the SU8 we obtain the best result possible. Therefore, a thorough hard bake process is necessary as illustrated in Figure 3.12.

Figure 3.12: SU8 on silicon squares 2x2 cm after the sputtering process, in the left side the SU8 was hard-baked while on the right it is not

However, the formation of the bubbles on the chip occurs only in the zones where the patterned cladding area is bigger. This suggests that these regions retain a relatively higher amount of solvent compared to other parts. To overcome this problem, we optimize the cladding layout using KLayout software (Figure 3.13a). The objective was to reduce the size of these larger regions paying attention to the exponential decay of the optical field in the waveguide. With all the previous changes in mind, we repeated the deposition process, resulting in the elimination of bubbles (as shown in Figure 3.13b).

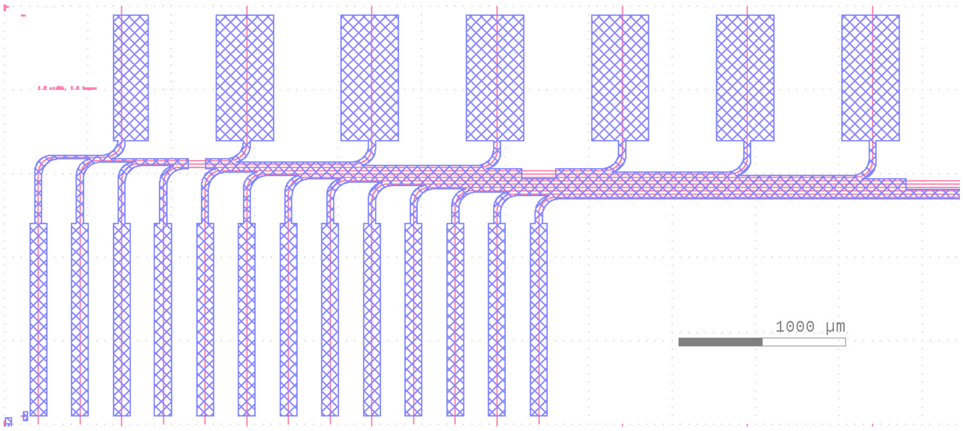

(a)

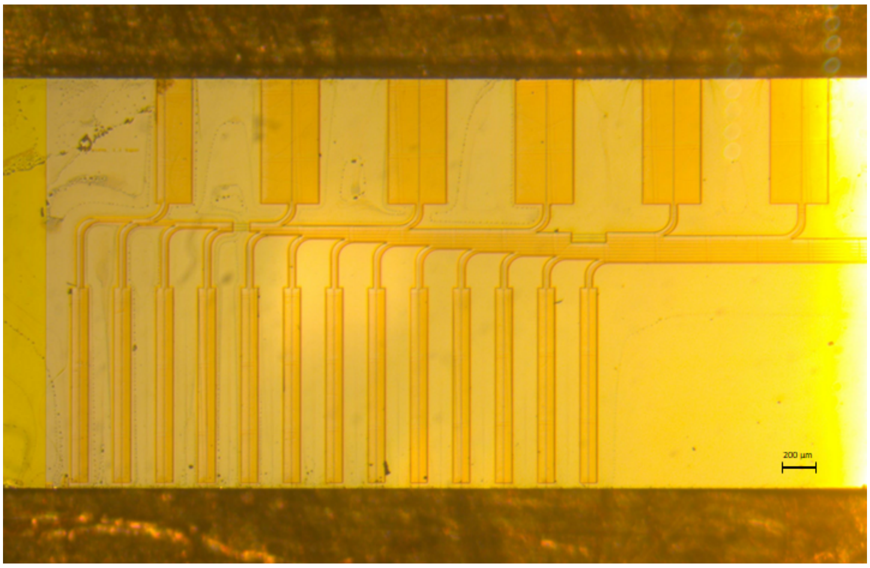

(b)

Figure 3.13: In (a) the final design of the chip from KLayout, while in (b) the chip after the sputtering deposition without bubbles.

3.4. Optical characterization

With the optimal chip without any bubbles, we have to test the performance of the device. The task is to measure the insertion losses of the device. Measuring the insertion losses is important to understand how the silicon oxycarbide affects the performance of the chip. From simulations, the insertion losses expected for a silicon oxycarbide characterized with the ellipsometer is 0.042 dB/μm. Thus, in the process of coupling, we used an edge-coupling setup with lensed fibers. The input lensed fiber was connected to an infrared (IR) laser and a polarizer. While the output lensed fiber has to collect the light exiting from the waveguide and it is connected to a photodetector, to gauge the light intensity from the waveguides. Both fibers were mounted on three-axis stages to enable accurate micrometric control over their positioning. Upon coupling the light, we conducted adjustments to maximize the power level by finely tuning the positioning of the fibers. A simplified scheme of our experiment is represented in Figure 3.14. As mentioned before the SiOC is deposited on the uncladded windows of our chip. The waveguides used have windows lengths equal to 100 μm and 200 μm. We know that the insertion losses of the light into the waveguide with only SU8 cladding are 3 dB/cm. The results obtained from the experiment are presented in Table 3.3

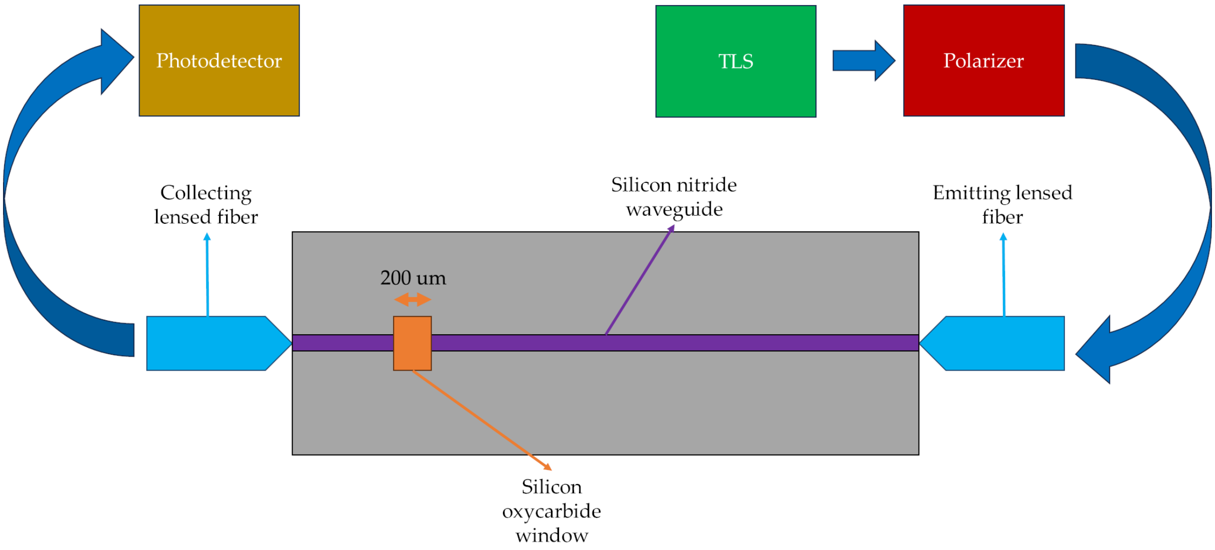

Figure 3.14: A simple scheme of the setup used for the experiment with all the connections of the fibers

Waveguide length (cm)	**Window window (μm)**	**Power received normalized (dB)**
0.29	-	-10.87
0.34	100	-15.02
0.39	100	-17.17
0.44	100	-20.32
0.49	200	-23.47
0.54	200	-30.62
0.59	200	-26.77

Table 3.3: All the transmission measurements of the chip without SiOC and with it

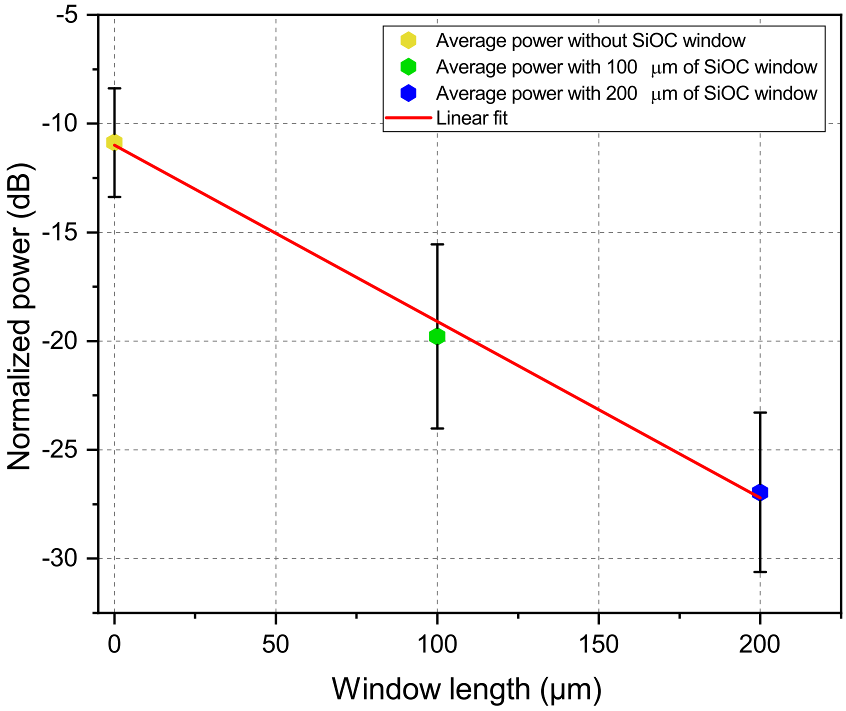

Figure 3.15: The trend of the power received vs the SiOC windows lengths. The slope (equal to 0.083 dBm/μm) is the absorption of the SiOC

As evident from the results, the silicon oxycarbide windows exhibited absorption of the incoming power entering the waveguides equal to 0.083 dBm/μm in average (shown in Figure 3.15, a value almost double with respect to the simulations. Therefore, a trade-off of SiOC cover must have been done to guarantee an efficient phase shift of the wave and to have the minimum losses possible. Considering that the insertion losses are directly related to the extinction coefficient we obtain a value of k which is double with respect to the ellipsometry analysis.

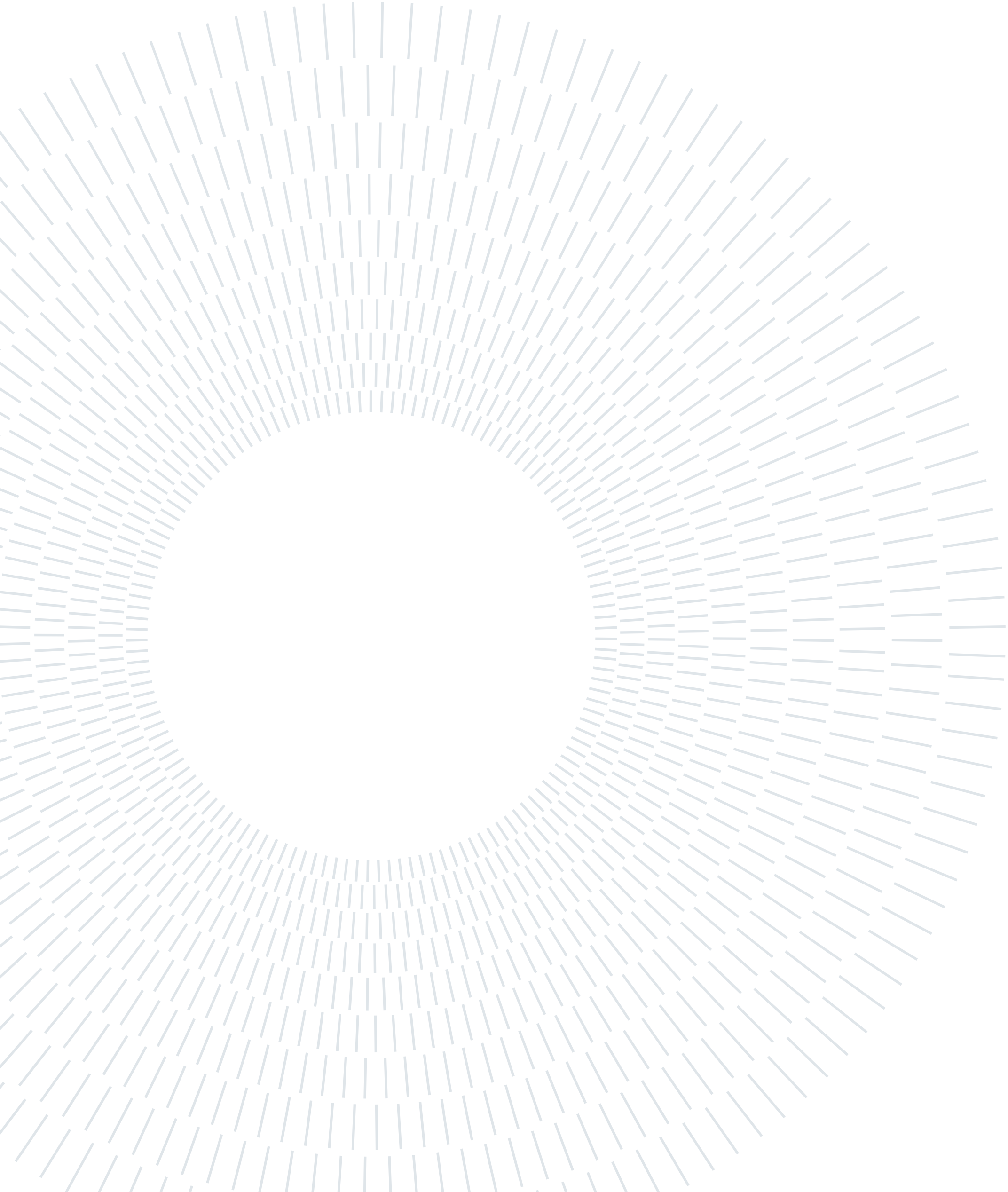

4 | Thermo-optic analysis

4.1. Thermo-optic coefficient

The refractive index is a material property it changes with physical quantities like temperature. The so-called thermo-optic coefficient is the variation of the refractive index in temperature at constant pressure $\frac{dn}{dT}$ and the unit of measure is $°C^{-1}$. The values of thermo-optic coefficients of the materials used in photonics are very small and span from 10^{-6} to 10^{-3} and can also assume negative values [11]. Over the years, many models have been proposed to evaluate this property for all types of materials from a solid-state physics point of view. The most important model for glasses is described by Prod'homme [11] which links the thermo-optic coefficient with the thermal expansion coefficient (α) and the electronic polarizability (ϕ).

In integrated photonics, the thermo-optic coefficient is exploited to make thermal actuators to manipulate the light on the waveguide. The material with a high thermo-optic must have also a high refractive index to maximize the overlap of the fundamental mode. In our application, the silicon oxycarbide will be deposited on top of a silicon nitride waveguide, so the fundamental mode of the waveguide will be overlapped with the SiOC material. Heating the silicon oxycarbide will change the effective refractive index of the mode, therefore the TE mode will phase shift depending on the length of the heater device and the temperature applied. From previous works [18] the thermo-optic coefficient of the silicon oxycarbide is proven to be 2.5×10^{-4} $°C^{-1}$

The main task of our work is developing a reproducible way to make silicon oxycarbide, so a test of the thermo-optic is needed. Thus, we propose two types of experiments to find the thermo-optic coefficient, one regarding thin film reflectometry and the other one regarding measurements on integrated chip.

4.2. SiOC thin film reflectometry

The general idea of this experiment is to use reflectometry to analyze how the refractive index of the thin films changes with temperature. According to Fresnel's equations if the incident light is reflected with an incident angle ≈ 0° we can consider the reflection coefficients to be independent with respect to the polarization. In Figure 4.1 is shown the ideal configuration for our experiment. To find the effective shift due to the thermo-optic coefficient we made a sweep of wavelength to define a harmonic response on our measurements. The thin film is considered as a Fabry-Perot cavity. In optics, a Fabry–Pérot is an optical cavity made from two parallel reflecting surfaces in which the optical waves can pass through the optical cavity only when they are in resonance with it. The interfaces between the optical fiber and silicon oxycarbide and with the last and silicon are considered as reflecting surfaces.

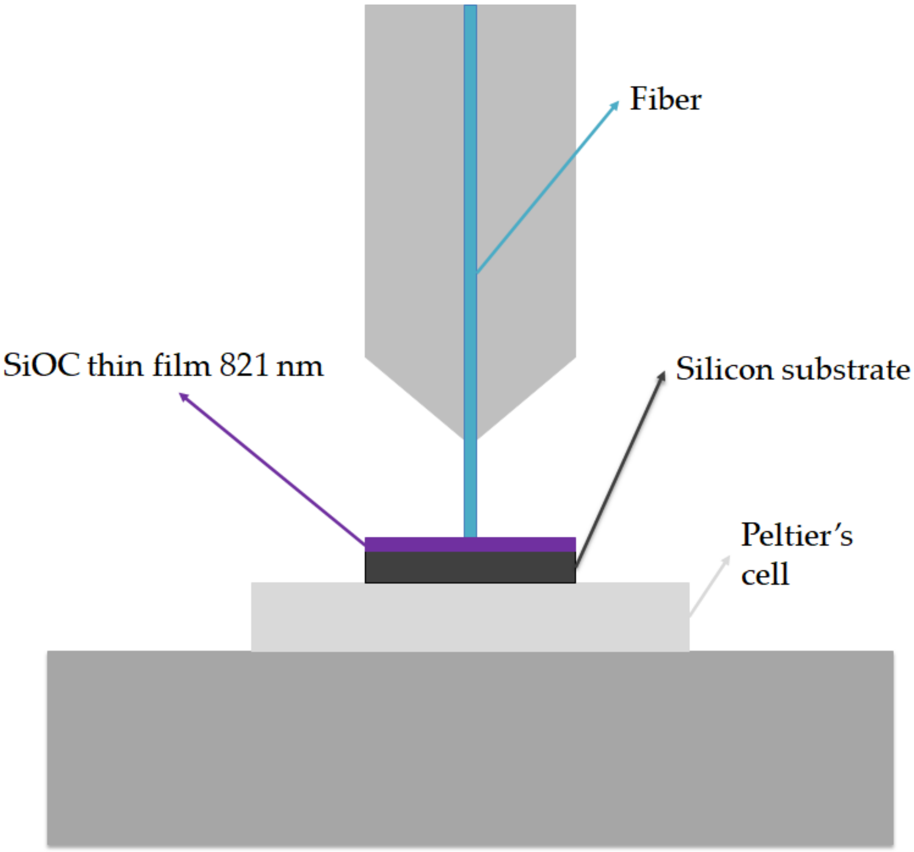

Figure 4.1: A scheme for the thin film experiment, a fiber is placed vertically, perpendicularly, and in contact with the SiOC thin film. With this configuration we can use Fresnel's law at 0° incidence angle

To make the experiment we described we put an optical fiber vertically thanks to a three-axis stage which has dual functionalities to keep it perpendicular to the thin film and to change the vertical direction sensitively. The fiber is in contact with the thin film to avoid any air cavities which can change the spectral response. To observe the actual position of the fiber with respect to the substrate an optical microscope, connected to a cam, is set horizontally, and through Motic Image Plus software it is possible to see if it is touching the substrate. On one side of the fiber, we remove all the fiber protective layer, clean the fiberglass with IPA, and cut it to obtain a surface as flat as possible (the magnification of the fiber is shown in Figure 4.3). The thickness of the thin film is 821 μm and the refractive index is measured to be 2.41 using the ellipsometer. The substrate is placed on an aluminum block which in turn is placed on a Peltier's cell module. The Peltier's cell is connected to a temperature controller to set the temperature of the system (as shown in Figure 4.2). A tunable laser source (TLS) in the NIR is used as a light source and it is connected through a fiber with a circulator which directs the light generated to the fiber in contact with the thin film. The reflected light will pass through the same fiber and the circulator will direct it to an optical spectrum analyzer (OSA) which will generate the spectral response we need. Before connecting the system to the OSA we have to measure the effective signal received through a photodetector until we obtain the optimal power obtainable without strong oscillations due to the vibrations of the fiber. A simple scheme of the setup is depicted in Figure 4.4

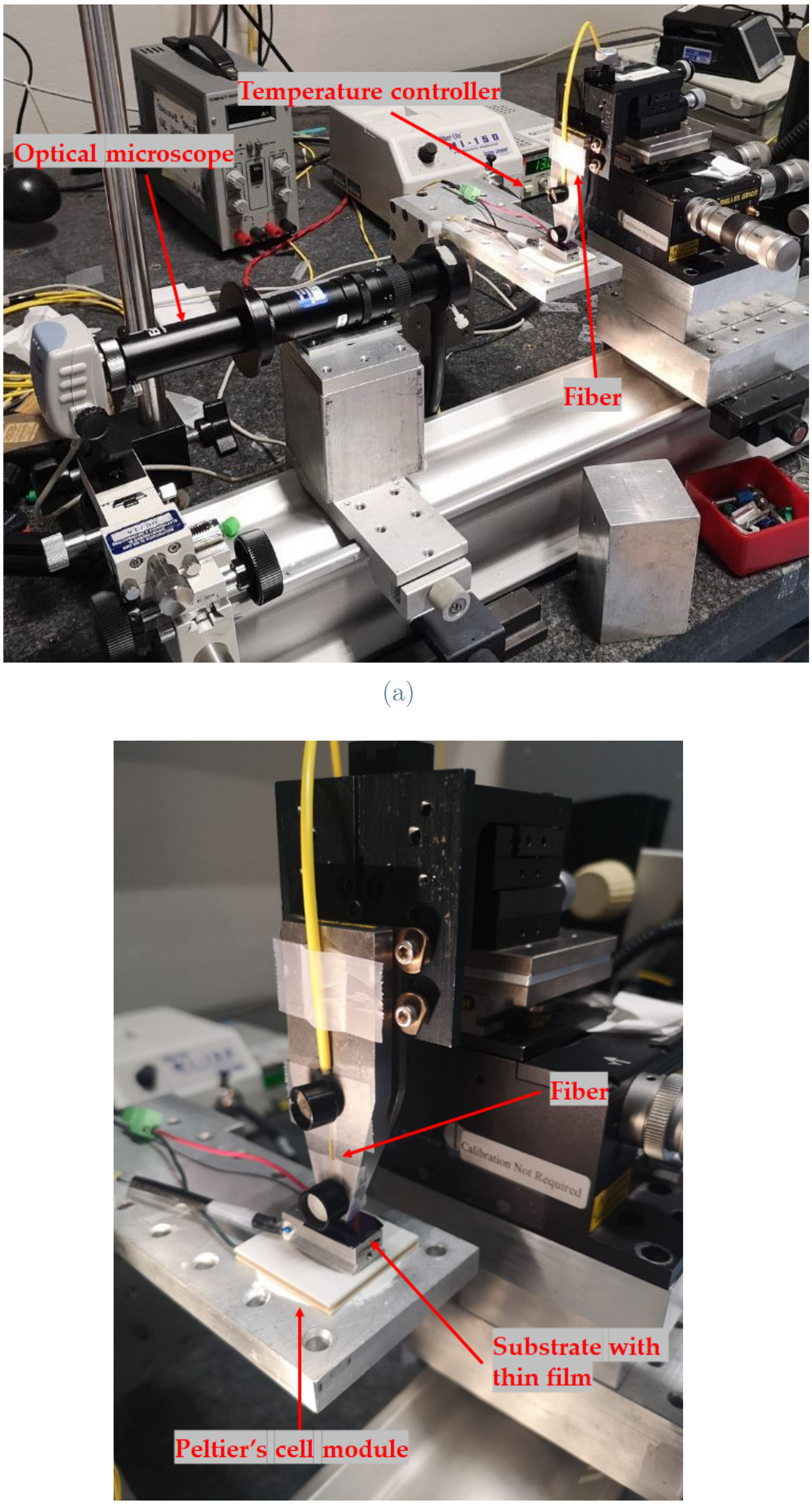

(a)

(b)

Figure 4.2: In (a) the setup with the optical microscope, while in (b) the vertical optical fiber with the substrate below

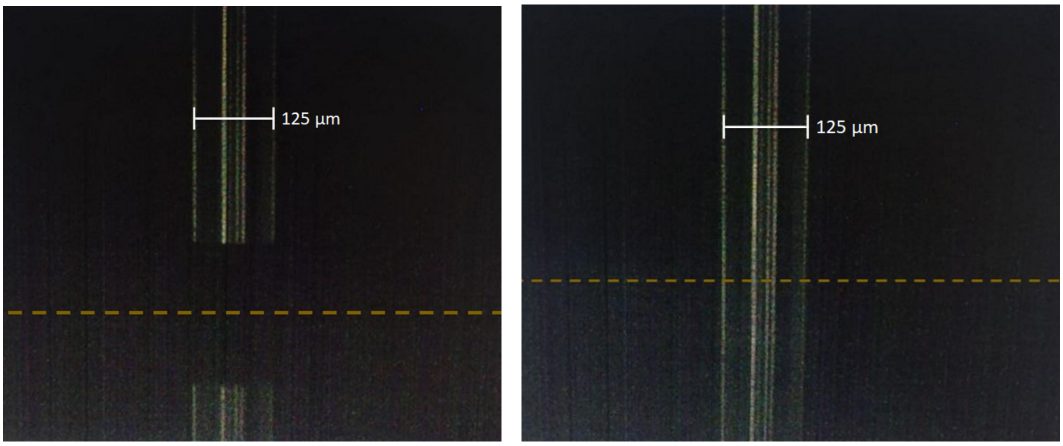

(a) (b)

Figure 4.3: Side view image through the microscope where we show (a) the fiber approaching the sample from the top, and (b) the fiber in contact with the sample's top surface. The image below the yellow dashed line is the fiber's reflection from the sample.

4.2.1. Experiment and results

The reflection contributions between the thin film and the substrate are important. Before making the experiment we used a simulator provided by Filmetrics called Reflectance Calculator [1]. This software allows us to calculate the reflection spectra produced from thin film putting the right values of refractive index and the range of wavelength we are interested in. We put the values of the refractive index of the layers we are interested in as well as their thickness, and a 100 nm wavelength range from 1520 nm to 1620 nm which are the values typical in telecommunication. The thickness and the refractive index of the silicon oxycarbide thin film are selected considering the simulated spectra which in the middle of the wavelength range there is a minimum. We made another simulation with the refractive indexes plus the thermo-optic contribution of the silicon and silicon oxycarbide found in the literature with a temperature interval of 30°C. Thus, we have two plots of reflection spectra with two minima respectively shifted of ≈ 4.8 nm, therefore with our experiment we have to find a shift near to this value (the two spectra are depicted in Figure 4.5). To make the experiment we set the wavelength sweep with our laser with increment units of 0.2 nm to have 501 points in our reflection spectra. For the experiment, we set two values of temperature, respectively 17°C and 47°C, so an interval of 30°C is used. Therefore, we obtained three measures for both temperature configurations.

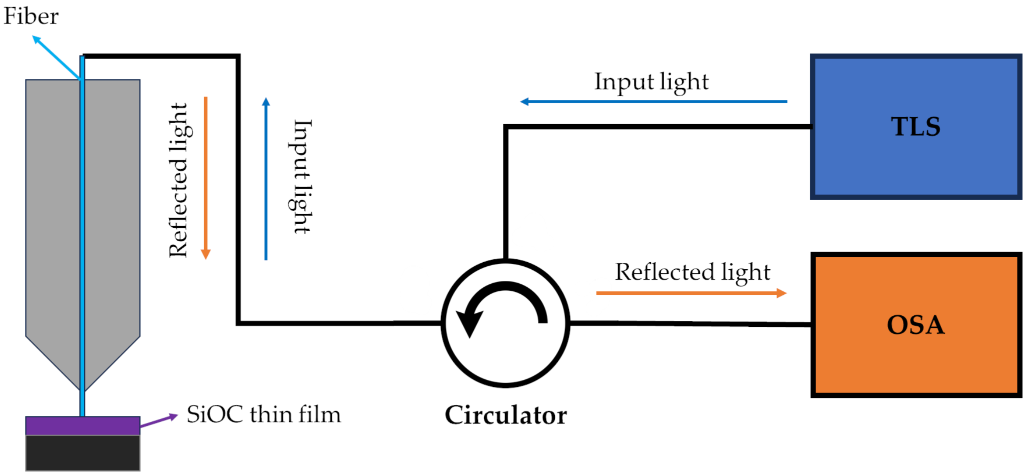

Figure 4.4: Simple scheme of the total setup used

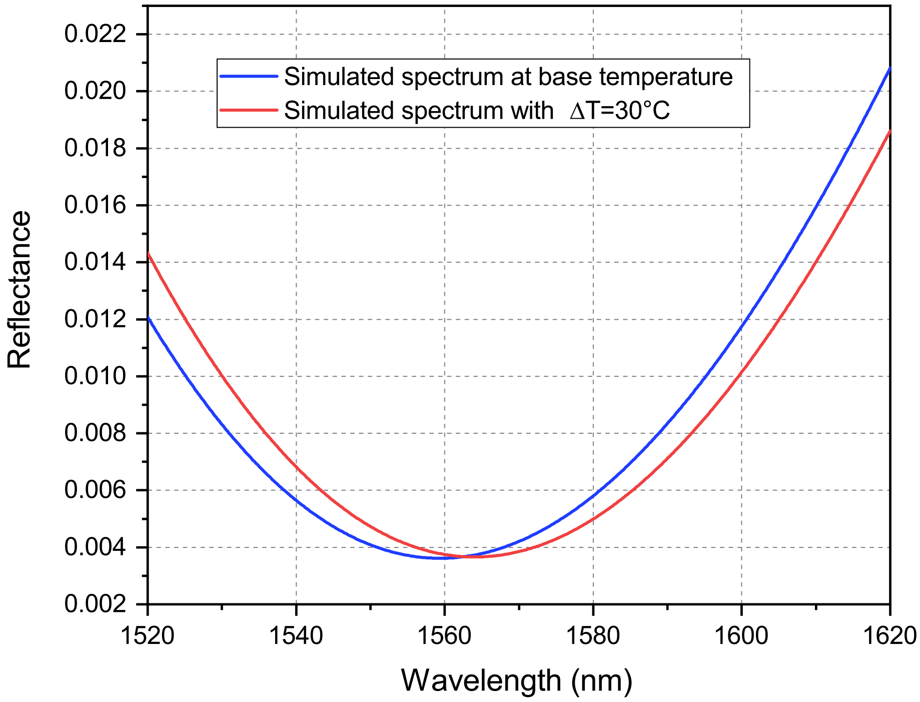

Figure 4.5: Simulated plot obtained from Filmetric Reflectance Calculator [1] considering the refractive index of SiOC equal to 2.41 and a thermo-optic coefficient of 2.5×10^{-4} °C^{-1}. We generate a plot at ambient temperature and another one at $\Delta T = +\ 30$°C.

4.2.2. Signal processing

The spectra we obtained (in Figure 4.6a) have a lot of peaks associated with noise which are unwanted signals that interfere with the communication or measurement of another signal. The noise sources are many and vary from audio frequency acoustic noise emanating from moving, vibrating, or colliding sources [34]. Thus, we have to filter to obtain the real response. To do so we use the Fast Fourier transform algorithm (through Matlab code) to calculate the discrete Fourier transform of a signal. Fourier analysis converts a signal which in our case is in the wavelength domain to a representation in the space domain. The Fourier transform of a signal points out all the harmonics whose is composed [20], so filtering the noise means, in this case, canceling all the signals with a low period in space. Furthermore, it points out the optical path of the reflected signals received, so all the peaks represent all the reflections received. If we take the two simulated spectra, apply the Fourier transform to the experimental ones, and measure the peaks we noticed that only the central one is in common (as shown in Figure 4.6b).

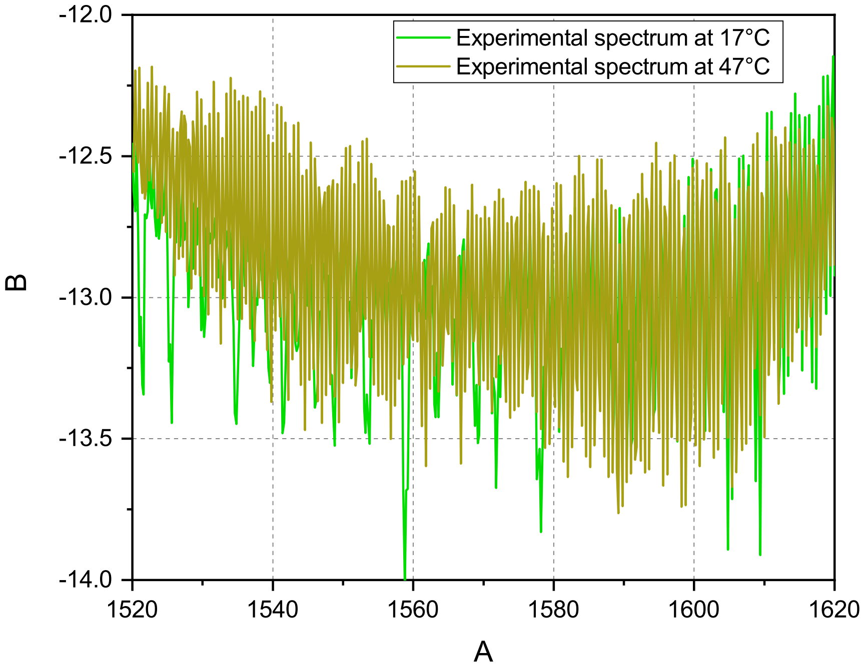

(a)

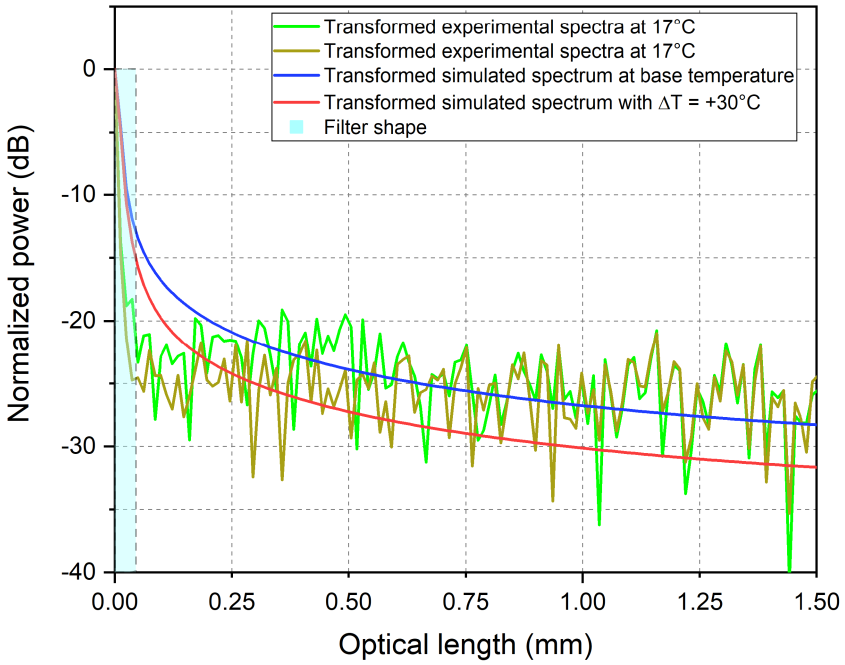

(b)

Figure 4.6: In (a) the experimental spectrum one for each temperature. While in (b) Fourier transforms of each experimental spectra with the low pass filter at 0.03 mm of optical length of bandwidth

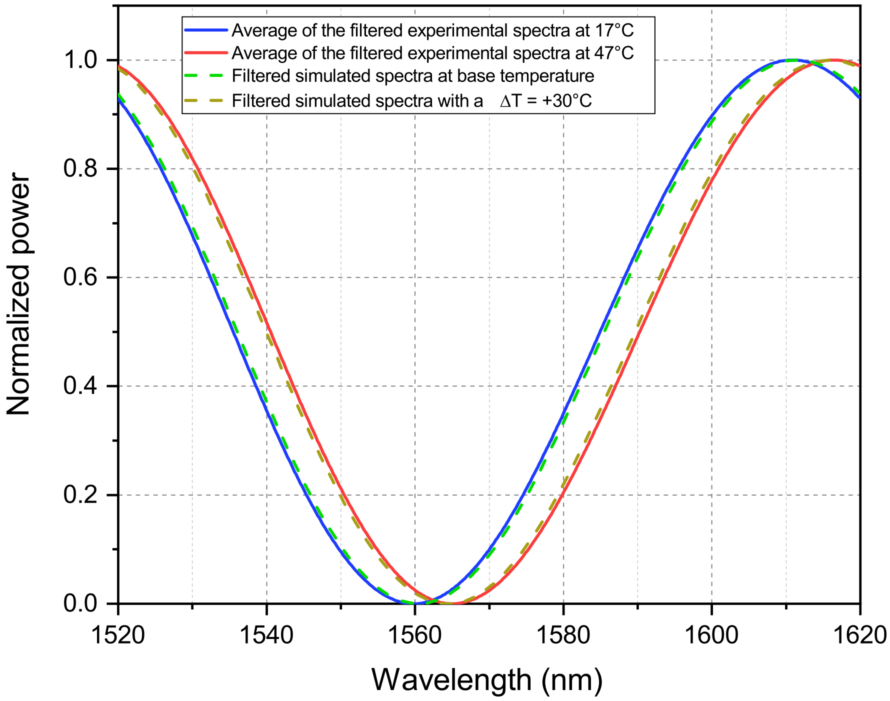

Figure 4.7: The experimental spectra obtained from the measurements

Thus, we use an ideal low pass filter with a band of 0.03 optical mm. We apply the IFFT (inversed fast Fourier transform) do an average of the experimental spectra filtered at their relative temperatures and normalizing with respect to the minima, we obtain experimental spectra almost equal to the simulated ones. If we analyze the wavelength shift we can notice a shift caused by the temperature of 5.1 nanometers which corresponds to $\approx 2.6 \times 10^{-4}$ $°C^{-1}$. Thus, the thermo-optic value found aligns with what we found in the literature. (as shown in Figure 4.7).

4.3. SiOC chip measurements

To calculate the thermo-optic coefficient in the silicon nitride waveguide platform we make transmission experiments on the chip we covered of silicon oxycarbide in the previous chapter. The experiment involves coupling the chip with two lensed fibers in an edge-coupling configuration mounted on a three-axis stage to have a micrometric control of their position. To couple the fibers to the chip we used an optical microscope to see their exact position, and, as an alignment step, a red laser to see if the light interacts with the waveguide. The input fiber is responsible for the emission of the light, so is connected to a polarizer which in turn is connected to a tunable IR laser source. While the output fiber is responsible for collecting the light from the chip, so it is connected firstly to a photodetector to see if we can see any transmitted power and, after we reach the optimal value, it is connected to an optical spectrum analyzer (OSA) to see the signal response. The waveguide chosen for our experiment has a total length of 0.54 cm and a window length of 200 μm. In Figure 4.9 is shown a simple scheme of the setup which is really similar to the scheme of the fiber coupling section. As for the wavelength sweep we choose a range from 1520 nm to 1580 nm with incremental units of 5 pm to see more clearly the transform peaks. The chip is put onto an aluminum block just above a Peltier's cell module enabling the tuning of temperature. The temperature values are controlled with a temperature controller and we set values of temperature 17°C and 47°C, so a $\Delta T = 30$°C. The experimental spectra are shown in Figure 4.8

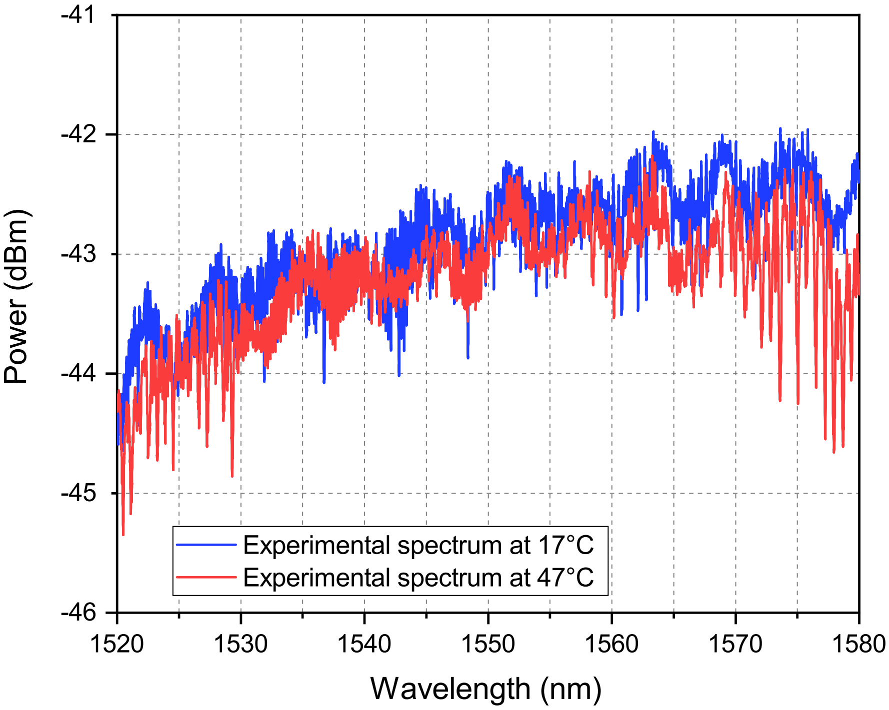

Figure 4.8: The experimental spectrum obtained from the measurements one for each temperature

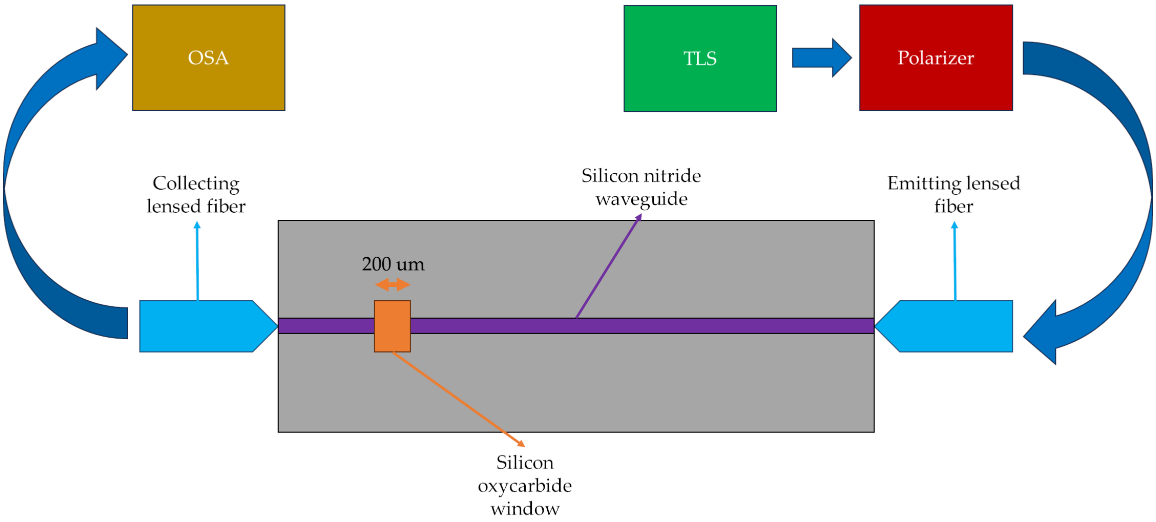

(a)

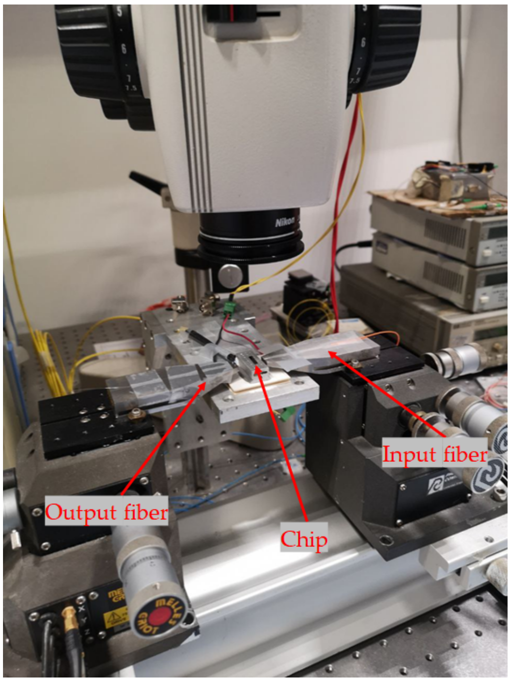

(b)

Figure 4.9: In (a) a simple scheme of the setup used for the experiment with all the connections of the fibers (b) the setup of the experiment

4.3.1. Experiment and results

Before the sweep, we made some simulations on the cross-sections of the chip to assess the fraction of power distribution of the mode in the waveguide (in Table 4.1 and Table 4.2). In the zone where there is the SU8 cladding the fundamental TE mode is well confined in the waveguide, while for the cross-section with SiOC on top the shape is overlapped from the waveguide (Figure 4.10). The modal effective indexes group and the velocity refractive index n_g of the TE mode in the window area and with SU8 cladding are respectively equal and 1.763, 1.533, 2.152, and 1.937.

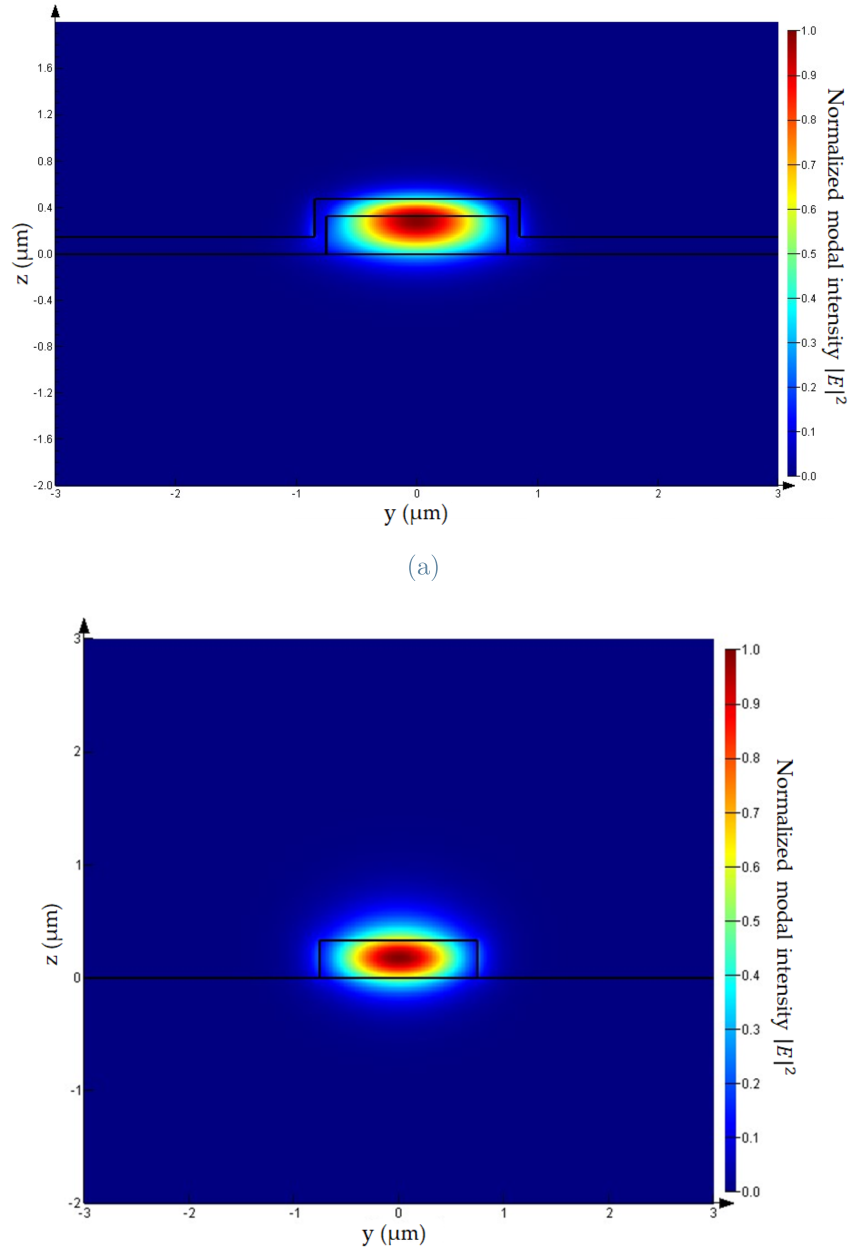

(a)

(b)

Figure 4.10: In (a) the modal intensity distribution of the window zone cross-section while in (b) the modal intensity distribution of the waveguide cross-section

Material	**Power fraction %**
Si_3N_4	55.296
Cladding (SU8)	28.982
Substrate (SiO_2)	15.721

Table 4.1: Power fraction for the cross-section with SU8 on top

Material	**Power fraction %**
Si_3N_4	58.089
SiOC	24.854
Substrate (SiO_2)	9.604
Air	7.452

Table 4.2: Power fraction for the cross-section with SiOC on top

The experiment consists of measuring the transmission spectral response of the chip. As in the previous experiment, we will filter the experimental signals obtained. We have to consider the variation of the optical path due to the silicon oxycarbide window cavity. The silicon oxycarbide has a higher refractive index with respect to the rest of the chip, so the actual representation of the peaks of the Fourier transform is the optical paths of the beam with the reflection contributions of the optical cavities generated by the window in the chip. Thus, we have to take the peak related to the entire window length cavity (which is considered a Fabry-Perot cavity) and filter those peaks and the central one with three ideal bandpass filters with bandwidths respectively of 0.06 mm and 0.12 mm as shown in Figure 4.11a. The x-axis of the Fourier transform plot describes the optical path of the beam, so to obtain the real length, we have to divide for n_g. To confirm that the peaks of the FFT belong to the measures we did, we do a confrontation between the spectra of the waveguide without a window and those with the window. The reflection induced by the windows is not enough to see any peaks, but it is possible to see a peak at 10.33 mm relative to the cavity representing the length of the entire chip. To confirm the measure, we do other experiments with the waveguide without the window to confront the spectra and to find any interesting peaks (Figure 4.11a and Figure).

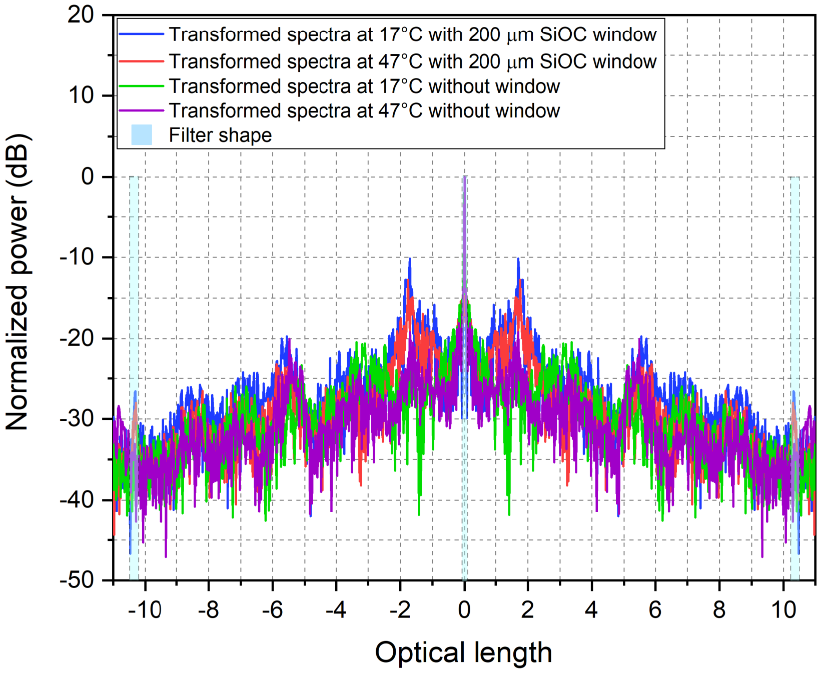

(a)

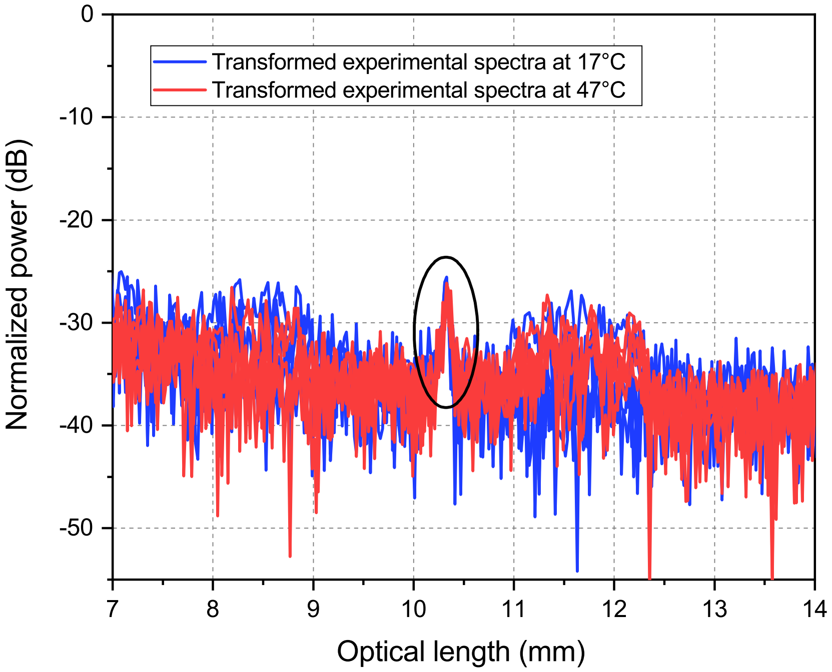

(b)

Figure 4.11: In (a), the total FFT spectra and the shape of the ideal bandpass filters with a bandwidth of 0.06 optical mm for the central peak and 0.12 optical mm for the other two. In (b), the magnification on the secondary peak

To obtain the shift of the spectra through temperature, we have to calculate every contribution of thermo-optic variation of $\Delta T = +30°C$ in the chip (in Table 4.3) there are all the materials of the chip with their thermo-optic coefficient). To obtain the thermo-optic of the two cross-sections we have to see the variation of the modal effective index. Through simulations, we calculated a Δn_{eff} of the window of $\approx 2.454 \times 10^{-3}$ which corresponds of a thermo-optic coefficient equal to 8.2×10^{-5} $°C^{-1}$ and a Δn_{eff} of the wavelength with SU8 of $\approx -4.92 \times 10^{-4}$ which corresponds of a thermo-optic coefficient equal to -1.64×10^{-5} $°C^{-1}$. To obtain the thermo-optic of the entire structure, we do a weighted average of the two contributions considering the two lengths (0.2 mm of the window and 5.2 mm of the rest of the chip). The total thermo-optic obtained is $\approx -1.3 \times 10^{-5}$ so using the formula 4.1 we expect a negative shift ($\approx$ 0.3 nm) of the signals through.

$$\frac{\Delta\lambda}{\lambda} = \frac{\Delta n_{\text{eff}}}{n_{\text{g}}} \tag{4.1}$$

Material	**Thermo-optic coefficient ($°C^{-1}$)**
Si_3N_4	2.51×10^{-5}
Cladding (SU8)	-1.1×10^{-4}
Substrate (SiO_2)	1×10^{-5}
SiOC	2.6×10^{-4}

Table 4.3: Power fraction for the cross-section with SU8 on top

Filtering the signals, we measure a shift at 1550 nm, but the value doesn't correspond (-0.08 nm) as shown in Figure 4.12. Measuring the range of the period is equal to 0.14 nm, so the shift obtained from simulations is larger. Thus we don't know how many periods the signal shifted.

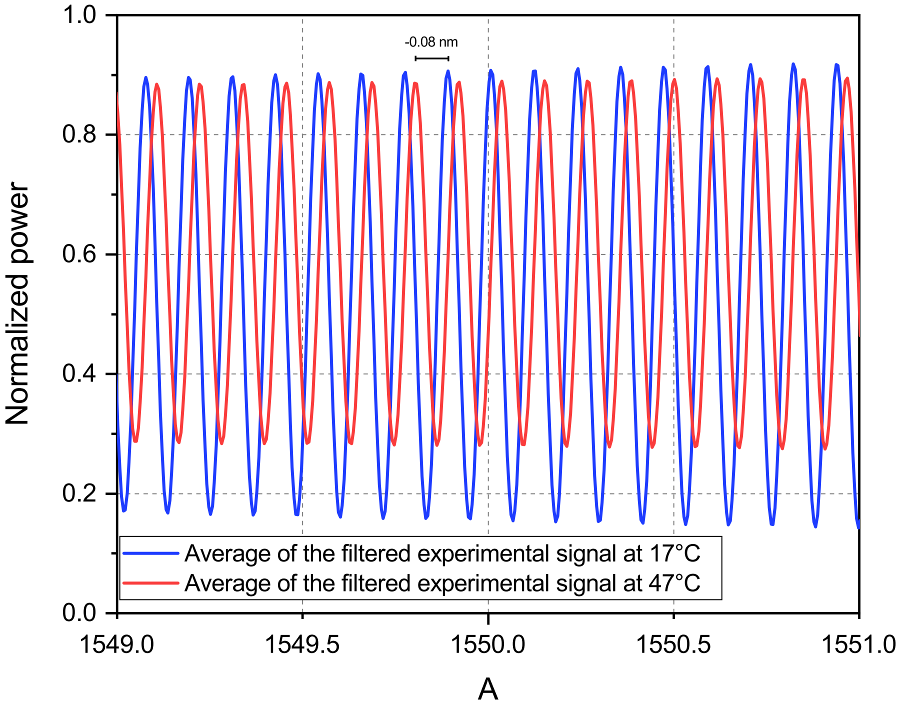

Figure 4.12: Filtered spectra with the negative shifts.

Conclusion: towards SiOC thermal actuator for integrated optics

This thesis aimed to develop, characterize and integrate thin film silicon oxycarbide on a photonic chip. Our objectives were to obtain a SiOC film with a refractive index of around 2.2 and a high thermo-optic coefficient in a reproducible way.

We experimentally showed the integration of the silicon oxycarbide onto a photonic chip. Our deposition recipe is compatible with a standard integrated photonic material, particularly a silicon nitride waveguide covered with SU8 photoresist. We characterized the SiOC performances on silicon nitride waveguide, measuring the propagation losses of 0.0826 dB/μm and a thermo-optic coefficient of 2.6×10^{-4} °C^{-1} which is indeed a high value that could improve the current state of the art of optical, thermal actuators.

This thesis has demonstrated the high potential of this material, so the next steps will be:

- Designing and implementing a thermal actuator with the material and techniques we developed in this work
- Further investigation of the chemical composition, morphology, density, and uniformity of the thin films.
- Searching a trade-off between reducing the insertion losses and having the minimum length of the SiOC strip on the waveguide for an efficient thermal actuation.

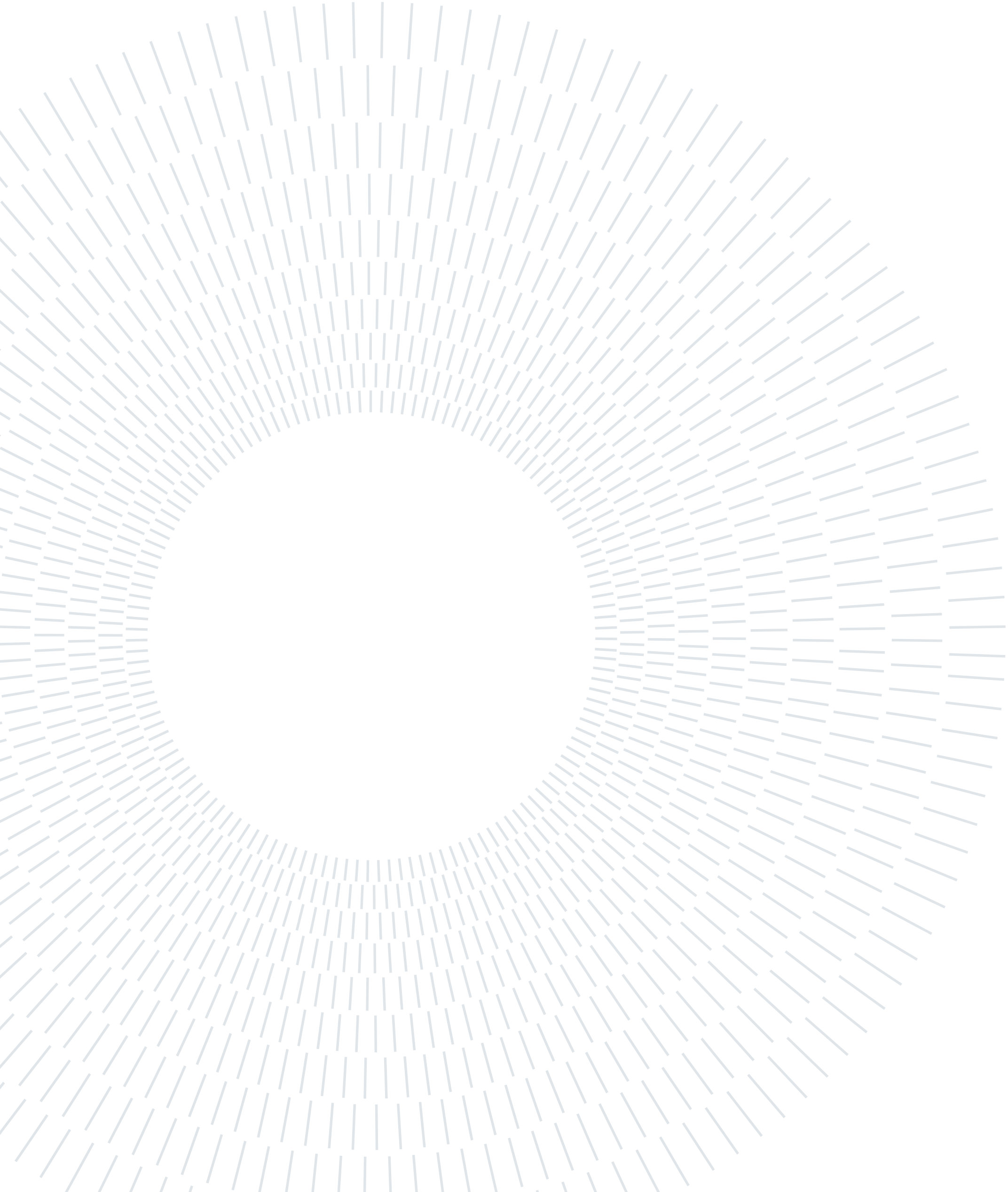

Bibliography

[1] URL `https://www.filmetrics.com/reflectance-calculator`.

[2] URL `https://www.jeppix.eu/`.

[3] URL `https://webbook.nist.gov/chemistry/`.

[4] URL `https://wiki.aalto.fi/display/SSC/Spin+coating`.

[5] K. Bawane, D. Erb, and K. Lu. Carbon content and pyrolysis atmosphere effects on phase development in SiOC systems. 39(9):2846–2854. ISSN 09552219. doi: 10.1016/j.jeurceramsoc.2019.03.032. URL `https://linkinghub.elsevier.com/retrieve/pii/S0955221919301918`.

[6] G. Beheim. Modern trends in microstructures and integrated optics for communication, sensing, and actuation. 36(5):1307. ISSN 0091-3286. doi: 10.1117/1.601331. URL `http://opticalengineering.spiedigitallibrary.org/article.aspx?doi=10.1117/1.601331`.

[7] A. A. Boiarski, J. R. Busch, B. S. Bhullar, R. W. Ridgway, L. S. Miller, and A. W. Zulich. Integrated optic biosensor. pages 15–26. doi: 10.1117/12.144843. URL `http://proceedings.spiedigitallibrary.org/proceeding.aspx?articleid=1007564`.

[8] E. J. L. Edward Cohen. *Kirk-Othmer Encyclopedia of Chemical Technology Coating Processes*. Wiley, West Sussex, 2011.

[9] R. Feng and R. J. Farris. Influence of processing conditions on the thermal and mechanical properties of SU8 negative photoresist coatings. 13(1):80–88. ISSN 0960-1317. doi: 10.1088/0960-1317/13/1/312. URL `https://iopscience.iop.org/article/10.1088/0960-1317/13/1/312`.

[10] H. Fujiwara. *Spectroscopic Ellipsometry: Principles and Applications*. Wiley, West Sussex, 2007.

[11] G. Ghosh. *Handbook of thermo-optic coefficients of optical materials with applications*. Academic Press. ISBN 978-0-12-281855-4.

[12] W. M. Green, M. J. Rooks, L. Sekaric, and Y. A. Vlasov. Ultra-compact, low RF power, 10 gb/s silicon mach-zehnder modulator. 15(25):17106. ISSN 1094-4087. doi: 10.1364/OE.15.017106. URL `https://opg.optica.org/oe/abstract.cfm?uri=oe-15-25-17106`.

[13] N. C. Harris, Y. Ma, J. Mower, T. Baehr-Jones, D. Englund, M. Hochberg, and C. Galland. Efficient, compact and low loss thermo-optic phase shifter in silicon. 22 (9):10487. ISSN 1094-4087. doi: 10.1364/OE.22.010487. URL `https://opg.optica.org/oe/abstract.cfm?uri=oe-22-9-10487`.

[14] R. G. Hunsperger. *Integrated Optics*. Springer New York. ISBN 978-0-387-89774-5 978-0-387-89775-2. doi: 10.1007/b98730. URL `http://link.springer.com/10.1007/b98730`.

[15] K. Ikeda, R. E. Saperstein, N. Alic, and Y. Fainman. Thermal and kerr nonlinear properties of plasma-deposited silicon nitride/ silicon dioxide waveguides. 16(17): 12987. ISSN 1094-4087. doi: 10.1364/OE.16.012987. URL `https://opg.optica.org/oe/abstract.cfm?uri=oe-16-17-12987`.

[16] D. S. Krishna Seshan. *Handbook of thin film deposition*. Elsevier. ISBN 978-0-12-812311-9.

[17] D. M. Mattox. *Handbook of physical vapor deposition (PVD) processing*. William Andrew, 2nd ed edition. ISBN 978-0-8155-2037-5.

[18] F. A. Memon, F. Morichetti, M. Cantoni, C. Somaschini, M. Asa, R. Bertacco, B. S. Chowdhry, and A. Melloni. Silicon oxycarbide platform for integrated photonics. 38 (4):784–791, . ISSN 0733-8724, 1558-2213. doi: 10.1109/JLT.2019.2948999. URL `https://ieeexplore.ieee.org/document/8879562/`.

[19] F. A. Memon, F. Morichetti, and A. Melloni. High thermo-optic coefficient of silicon oxycarbide photonic waveguides. 5(7):2755–2759, . ISSN 2330-4022, 2330-4022. doi: 10.1021/acsphotonics.8b00512. URL `https://pubs.acs.org/doi/10.1021/acsphotonics.8b00512`.

[20] c. S. B. Michael T. Heideman, Don H. Johnson. Gauss and the history of the fast fourier transform. pages 14–21. doi: 10.1016/S0039-6028(03)00412-6. URL `https://web.archive.org/web/20130319053449/http://www.cis.rit.edu/class/simg716/Gauss_History_FFT.pdf`.

[21] *SU-8 2000 Permanent Epoxy Negative Photoresist PROCESSING GUIDELINES FOR: SU-8 2000.5, SU-8 2002, SU-8 2005, SU-8 2007, SU-8 2010 and SU-8 2015*. Microchem. URL `www.microchem.com`.

[22] S. K. Mitra and S. Chakraborty. *Microfluidics and Nanofluidics Handbook*.

[23] V. Nikas, N. Tabassum, B. Ford, L. Smith, A. E. Kaloyeros, and S. Gallis. Strong visible light emission from silicon-oxycarbide nanowire arrays prepared by electron beam lithography and reactive ion etching. 30(23):3692–3699. ISSN 0884-2914, 2044-5326. doi: 10.1557/jmr.2015.346. URL `http://link.springer.com/10.1557/jmr.2015.346`.

[24] M. Ohring. Chapter 5 - plasma and ion beam processing of thin films. In M. Ohring, editor, *Materials Science of Thin Films (Second Edition)*, pages 203–275. Academic Press, second edition edition. ISBN 978-0-12-524975-1. doi: https://doi.org/10.1016/B978-012524975-1/50008-2. URL `https://www.sciencedirect.com/science/article/pii/B9780125249751500082`.

[25] C. G. Pantano, A. K. Singh, and H. Zhang. Silicon oxycarbide glasses.

[26] J. Parra, J. Hurtado, A. Griol, and P. Sanchis. Ultra-low loss hybrid ITO/si thermo-optic phase shifter with optimized power consumption. 28(7):9393. ISSN 1094-4087. doi: 10.1364/OE.386959. URL `https://opg.optica.org/abstract.cfm?URI=oe-28-7-9393`.

[27] P. Pokorný, J. Musil, P. Fitl, M. Novotný, J. Lančok, and J. Bulíř. Contamination of magnetron sputtered metallic films by oxygen from residual atmosphere in deposition chamber: Contamination of magnetron sputtered metallic films by oxygen from residual atmosphere in deposition chamber. 12(5):416–421. ISSN 16128850. doi: 10.1002/ppap.201400172. URL `https://onlinelibrary.wiley.com/doi/10.1002/ppap.201400172`.

[28] R. W. Powell. Thermal conductivity of selected materials.

[29] A. Ribeiro and W. Bogaerts. Digitally controlled multiplexed silicon photonics phase shifter using heaters with integrated diodes. 25(24):29778. ISSN 1094-4087. doi: 10.1364/OE.25.029778. URL `https://opg.optica.org/abstract.cfm?URI=oe-25-24-29778`.

[30] J. Roy, S. Chandra, S. Das, and S. Maitra. OXIDATION BEHAVIOUR OF SILICON CARBIDE - a REVIEW.

[31] E. Serpini, A. Rota, A. Ballestrazzi, D. Marchetto, E. Gualtieri, and S. Valeri. The

role of humidity and oxygen on MoS 2 thin films deposited by RF PVD magnetron sputtering. 319:345–352. ISSN 02578972. doi: 10.1016/j.surfcoat.2017.04.006. URL `https://linkinghub.elsevier.com/retrieve/pii/S025789721730350X`.

[32] A. C. Sparavigna. Thermal conductivity of the crystalline silicon.

[33] L. F. Thompson and J. M. G. Cowie. Introduction to microlithography. edited by l. f. thompson, c. g . willson and m. j. bowden, ACS symposium series no. 219, american chemical society, washington DC, 1983. pp. ix + 363, price £42.95 (USA & cunada), $51.95 (export). ISBN 0-8412-0775-5. 18(4):280–280. ISSN 1934-256X. doi: 10.1002/pi.4980180426. URL `https://onlinelibrary.wiley.com/doi/abs/10.1002/pi.4980180426`. _eprint: https://onlinelibrary.wiley.com/doi/pdf/10.1002/pi.4980180426.

[34] S. V. Vaseghi. *Advanced digital signal processing and noise reduction.* Wiley, West Sussex, second edition, 2000.

[35] C. D. Vita. Silicon oxycarbide for integrated photonics. Master's thesis, Politecnico di Milano, 2019.

[36] A. Yoshigoe and Y. Teraoka. Time resolved photoemission spectroscopy on si()-2×1 surface during oxidation controlled by translational kinetic energy of o2 at room temperature. 532-535:690–697. ISSN 00396028. doi: 10.1016/S0039-6028(03)00412-6. URL `https://linkinghub.elsevier.com/retrieve/pii/S0039602803004126`.

Ringraziamenti

Desidero esprimere la mia sincera gratitudine al Professor Melloni per avermi offerto l'opportunità di svolgere la mia tesi in un ambiente di alta competenza tecnica. La sua guida è stata fondamentale per il successo di questo lavoro.
Un ringraziamento speciale va al Professor Morichetti per il suo prezioso aiuto nei momenti critici durante il lavoro di tesi. La sua competenza e il suo supporto hanno contribuito in modo significativo alla mia comprensione e al progresso del progetto.
Un ringraziamento ai dottorandi di Photonic Device lab in particolare Oscar e Francesca per avermi indirizzato, supportato (e sopportato) durante il lavoro di tesi. Senza di voi mi sarei smarrito il primo giorno e soprattutto avrei fatto solo simulazioni.
Un amorevole ringraziamento va poi alla mia famiglia, in particolare i miei genitori e mio fratello per avermi supportato durante il mio intero percorso di laurea. Senza di voi non ce l'avrei mai fatta